UNIVERSITY OF CALIFORNIA

Los Angeles

Scattering Properties of Nonperiodic Metasurfaces

A dissertation submitted in partial satisfaction
of the requirements for the degree
Doctor of Philosophy in Electrical and Computer Engineering

by

Cheng Tao

2020

ABSTRACT OF THE DISSERTATION

Scattering Properties
of Nonperiodic Metasurfaces

by

Cheng Tao
Doctor of Philosophy in Electrical and Computer Engineering
University of California, Los Angeles, 2020
Professor Tatsuo Itoh, Chair

Metasurface is a two-dimensional array of subwavelength elements that can manipulate the physical fields on the surface. Conventional periodic metasurfaces may face some physical constraints. For example, in metasurface gratings, the existence of specular reflection governed by the diffraction equation can diminish the grating efficiency. Besides, it is difficult to control the diffraction lobes and polarizations of the scattered wave. To overcome these limitations, we realize that breaking the periodicity of the elements will provide more flexibility to manipulate the scattering properties.

In this dissertation, we propose metasurfaces consisting of nonperiodic group cells optimized for desired scattering behaviors. Each group cell includes several locally periodic elements that are characterized by their reflection phase response under TE/TM or CP illumination. We first present nonperiodic metasurfaces used for retroreflection of oblique incident wave with linear polarization (TE/TM) and circular polarization (CP). For CP wave, both handedness reversal and handedness preservation cases are demonstrated. In the following chapter, we present nonperiodic metasurface beam splitter for TE and TM

polarizations based on the same method. Last, we propose the anisotropic metasurface that can convert linear polarization to circular polarization. All the metasurface designs are implemented by PCB fabrication and can be easily scaled to millimeter-wave, THz, and optical frequencies.

The dissertation of Cheng Tao is approved.

Aydin Babakhani

Benjamin S. Williams

Yuanxun Wang

Tatsuo Itoh, Committee Chair

University of California, Los Angeles

2020

To my Family,

all the Teachers and Mentors in my life,

who show me a world with

so many possibilities and opportunities.

TABLE OF CONTENTS

LIST OF FIGURES

LIST OF TABLES

ACKNOWLEDGMENTS

First, I would like to express my deepest gratitude to my advisor Professor Tatsuo Itoh for his continuous guidance and support during my PhD study. His insights, creativity and enthusiasm have been invaluable to me in shaping my research direction and motivating me to pursue higher research goals. I feel so lucky and proud to finally become a member of the Dragon Gate Club.

I would like to thank Professor Ben Williams, Professor Ethan Wang, and Professor Aydin Babakhani, who serve as the committee members, for providing advice and improving the quality of this dissertation.

I would like to thank my fellow labmates in the Microwave Electronics Lab, including Mohammad Memarian, Yasuo Morimoto, Kirti Dhwaj, Xiaoqiang Li, and Haozhan Tian. Thanks to the supportive and stimulating lab environment built by them, I found my PhD journey-often described by others as full of stress and bewilderments-rather enjoyable and rewarding. Also, I would like to thank Minji and Anastasios for helping the fabrication and measurement in my projects.

Finally, I would like to thank my parents and my girlfriend for their unconditional support. Their encouragements and trust are the most important reason I can make all these achievements. I love you all.

VITA

2011–2015 B.S. in Electrical Engineering, Shanghai Jiao Tong University, Shanghai, China

2015–2017 M.S. in Electrical Engineering, University of California, Los Angeles (UCLA), California, USA

2017–2020 Graduate Student Researcher, Department of Electrical and Computer Engineering, UCLA.

2020 Teaching Assistant, Department of Electrical and Computer Engineering, UCLA.

PUBLICATIONS

C. Tao and T. Itoh, "Nonperiodic Metasurfaces for Retroreflection of TE/TM and Circularly Polarized Waves," in IEEE Transactions on Antennas and Propagation, vol. 68, no. 8, pp. 6193-6203, Aug. 2020, doi: 10.1109/TAP.2020.2995324.

C. Tao, A. Papathanasopoulos and T. Itoh, "Linear-to-Circular Polarization Converter Based on Stacked Metasurfaces with Aperture Coupling Interlayer", presented at 2020 IEEE MTT-S International Microwave Symposium (IMS), Los Angeles, CA, USA, 2020.

C. Tao and T. Itoh, "nonperiodic Metasurface Beam Splitter for Dual Polarizations," 2019 49th European Microwave Conference (EuMC), Paris, France, 2019, pp. 670-673, doi: 10.23919/EuMC.2019.8910674.

C. Tao and T. Itoh, "nonperiodic Metasurface for Retroreflection of Circularly Polarized Wave," 2019 IEEE MTT-S International Microwave Symposium (IMS), Boston, MA, USA, 2019, pp. 35-38, doi: 10.1109/MWSYM.2019.8700999.

C. Tao, X. Li and T. Itoh, "Two-Dimensional nonperiodic Metasurface for Dual Polarization Retroreflection," 2018 48th European Microwave Conference (EuMC), Madrid, 2018, pp. 1194-1197, doi: 10.23919/EuMC.2018.8541665.

C. Tao, M. Memarian and T. Itoh, "A metasurface assisted half-mode leaky waveguide," 2017 47th European Microwave Conference (EuMC), Nuremberg, 2017, pp. 779-782, doi: 10.23919/EuMC.2017.8230963.

C. Tao, M. Memarian, Y. Morimoto and T. Itoh, "nonperiodic metasurfaces for blazing and beam splitting," 2016 Asia-Pacific Microwave Conference (APMC), New Delhi, 2016, pp. 1-4, doi: 10.1109/APMC.2016.7931287.

CHAPTER 1

Introduction

Metamaterials are artificial materials engineered to have properties not found in nature, such as negative-index materials [1, 2, 3, 4, 5, 6], and zero-index materials [7, 8]. As planar type metamaterials, metasurface is typically a composite layer engineered by an array of small scatterers or apertures to control the behaviors of physical fields on the surface, such as the wave front [6, 9, 10], surface impedance [11, 12] and phase [13, 14] from radio frequency to optical frequency. The thickness of the material layer is negligible with respect to the wavelength. Subwavelength elements are used to form the building blocks for the metasurface. Compared to 3D metamaterials, metasurfaces are compact, lightweight, and easy to fabricate. With these properties, metasurfaces have been applied in electromagnetic absorbers [15], waveguide structures [16] and wave focusing structures [13, 17], to name a few.

Among these applications, retroreflection of oblique incidence plane wave has been of particular interest to various regimes such as satellite communication, radar cross section (RCS) modification [18], remote sensing and Littrow external cavity laser [19]. Retroreflection of oblique incident wave has been traditionally achieved by 3D structures, such as metallic corner cube [20],[21] and metallic sawtooth gratings [22]. However, they are bulky and not suitable for planar fabrication. It is known that some retrodirective arrays such as phase conjugate array [23, 24, 25] and Van Atta array [26] can achieve broad angles of retroreflection. However, the former involves active components such as mixers and local oscillators, which increases the cost and complexity of fabrication and is unable to scale to high frequency. The latter is composed of antenna elements connected in pairs by transmis-

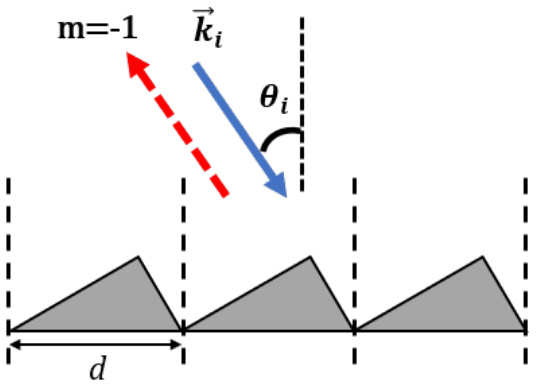

(a)

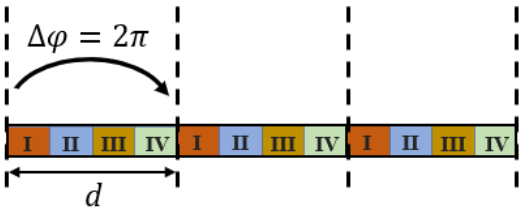

(b)

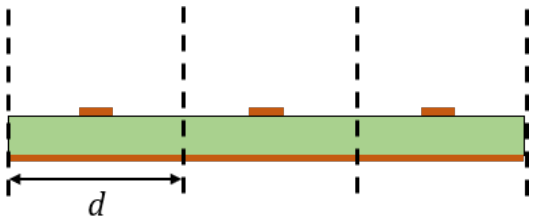

(c)

Figure 1.1: Several classic gratings structures for retrorefleciton of wave. (a) sawtooth gratings. (b) blazed metasurface gratings. (c) resonant blazed gratings.

sion lines. This configuration usually requires multi-layer structures and the transmission lines need to be aligned symmetrically to the array center. When the number of elements increases, the routing of antenna elements becomes more complicated and will bring about extra loss. Again, it is difficult to incorporate this array in the designs of THz or optical devices.

Recently, metasurface gratings have been experimentally demonstrated to achieve retroreflection [27, 28, 29, 30, 31, 32, 33]. Fig. 1.1 shows some examples that can be regarded as planar equivalence of sawtooth gratings. In metasurface gratings, the unit cell is designed in planar fashion, usually based on a single layer structure, using either periodic phase-modulating elements or periodic planar resonant cells. All feasible gratings are finite in size, which may be in the order of tens or hundreds of periods, depending on the application and operation frequency.

The governing equation of a one-dimensional grating for propagating waves in vacuum can be expressed as [34]:

$$sin(\theta_i) + sin(\theta_m) = \frac{m\lambda_0}{d}, \tag{1.1}$$

where d is the periodicity of the gratings, m is diffracted order, λ_0 is operating wavelength, θ_i is incidence angle, and θ_m is diffracted angle. Both θ_i and θ_m are negative values if the incident and diffracted beams are on the left hand side of the grating surface normal in Fig. 1.1.

For retroreflection of the wave, the periodicity of the gratings must be chosen to force the diffraction angle of $m = -1$ mode to be in the direction of incidence ($\theta_m = \theta_i$), thus satisfying:

$$kdsin(\theta_i) = \pi \tag{1.2}$$

where k is the wave number in free space. This is also known as Bragg condition, causing the beam to be directed back in the path of incidence. The angle of incidence will determine the periodicity of the grating.

However, we know that the specular reflection ($m = 0$ mode, $\theta_m = -\theta_i$) for gratings automatically exists as the specular model is always a valid solution in equation (1). The scattered wave is therefore usually a combination of both $m = 0$ and $m = -1$ diffraction order. The existence of specular reflection or other diffraction mode is in practice a challenge with blazed gratings, which has led to a great body of literature on grating efficiency [35, 34]. A complete treatment of grating efficiency requires that vector formulation of electromagnetic theory applied to the grating surface. The distribution of the power by the grating depends in a complicated way on the element spacing and profile, the spectral order, the wavelength and the grating material. Although high retroreflection (or $m = -1$ mode) efficiency can still be achieved in all-dielectric gratings with multi-layers nanofabrication [36, 37] or carefully designed unit cells with resonant condition [30]. It is still desirable that we develop a simpler model based on planar fabrication to manipulate the retroreflection properties, such as specular reflection power level, beamwidth and wave polarization. Moreover, the design method should be transferable to all frequencies.

To deviate this traditional grating design methodology, we realize that breaking the periodicity of elements will give us more flexibility to manipulate the scattered wave through optimization process. For accurate element modeling, periodic boundary condition (PBC) is still required. This can be approximated by putting identical elements inside a group cell or in one dimension [38], but the entire surface will appear in nonperiodic fashion by optimizing group cells or elements alignment along the other dimension.

To construct such metasurface, we first treat the metasurface aperture of finite size as a 2D subwavelength scattering arrays of the basic elements with equal center to center spacing. Several adjacent basic elements are set identical to each other to form a group cell. This locally periodic configuration will ensure that the elements inside one group cell can be characterized by the same phase response with great accuracy, which can be easily extracted from full wave simulation. The group cells are arranged in nonperiodic fashion along the entire aperture to achieve the desire scattering behavior, without being

restricted by the grating equations. Thanks to the theoretical scattered pattern model, this nonperiodic metasurface design simply requires a primary genetic algorithm, which greatly reduces the computational complexity. This contrasts with many metasurfaces designed by optimization that combines the genetic algorithm with a more complicated full wave EM solver to determine the metasurface geometry [39]. Therefore, one can have access to the optimal design of thousands of subwavelength elements within reasonable amount of time.

In the next chapter, we will present the theory based on high impedance surface and phased arrays to model the nonperiodic metasurface[40]. In chapter 3, we will apply the nonperiodic design method to achieve retroreflection of TE and TM polarizations simultaneously, and furthermore circular polarization[41, 42]. Chapter 4 will extend this design to the application of beam-splitting, to demonstrate the flexibility of this method[43]. In chapter 5, a supplementary prototype of linear-to-circular polarization converter will be proposed based on the anisotropic metasurface[44].

CHAPTER 2

Theory and Methodology of Nonperiodic Metasurfaces

Fig. 2.1 shows the schematic of the nonperiodic metasurface. We assume that the incident wave impinges on the board from the angle $\theta_i = -30^\circ$ in $\phi = 0^\circ$ plane (or xz plane), indicated by the solid arrow. To be consistent with the diffraction gratings notation, scattered wave angle θ_r (dashed arrow) is defined negative if the angle is on the left hand side of surface normal in Fig. 2.1. In this figure, electric field of TE wave is polarized along y-axis and electric field of TM wave is polarized in in $\phi = 0^\circ$ plane, perpendicular to the incidence direction. In the beginning, we discretize a piece of finite surface into many subwavelength basic elements that line up in both x- and y- dimension as shown in Fig. 2.1. Center to center spacing is set to be a fixed value d. A cluster of 3×3 or 4×4 identical basic elements will form a group cell, so that approximately each basic element will meet the periodic boundary condition. Under this assumption, we are going to use transmission line model to characterize these locally periodic basic elements by the TE/TM surface impedance, which can be used to derive reflection coefficients or reflection phase. Using the phase response of different basic elements, we can further construct the scattered far field pattern of the whole metasurface.

Fig. 2.2 shows the equivalent transmission line model to calculate the reflection coefficient of such periodic basic elements [45, 46]. In this model, we assume the element is made of metal on top of metal-backed dielectric with thickness h and dielectric constant ε_r. It can be conveniently characterized by a transmission line of length h with short circuit at the end. This piece of transmission line along with the top metallization will contribute to the

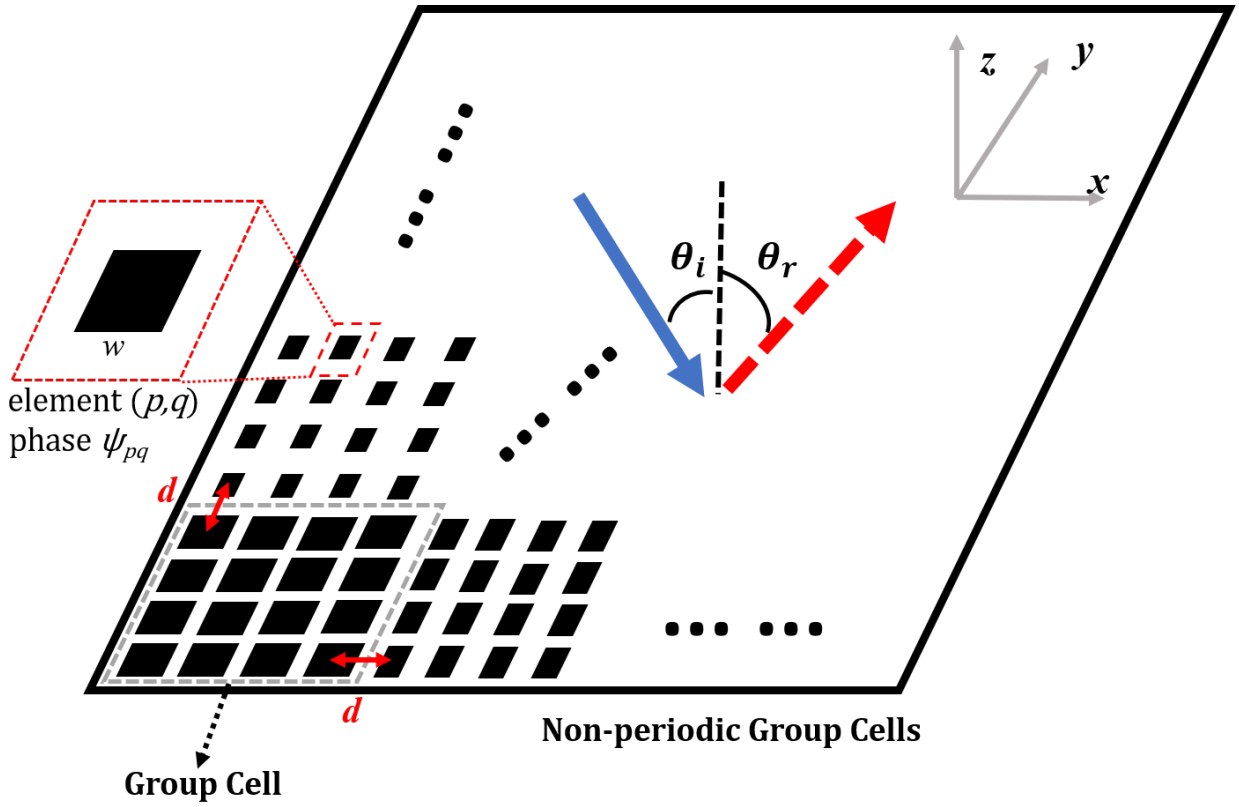

Figure 2.1: Schematic of nonperiodic metasurface. Solid arrow indicates incident wave and dashed arrow indicates scattered wave.

surface input impedance. If we only consider two directions of wave propagation, incoming incidence direction and reflection direction, the reflection coefficient Γ_s will characterize the mismatch between the free space wave impedance and the input impedance of the surface. For TE and TM cases, the wave impedance can be expressed as:

$$Z_0^{TE} = \frac{Z_0}{\cos\theta_i} \tag{2.1}$$

$$Z_0^{TM} = Z_0 \cos\theta_i \tag{2.2}$$

where Z_0 is free space plane wave impedance and θ_i is the incidence angle. The input surface impedance Z_s^{TE} and Z_s^{TM} can be determined by the equations:

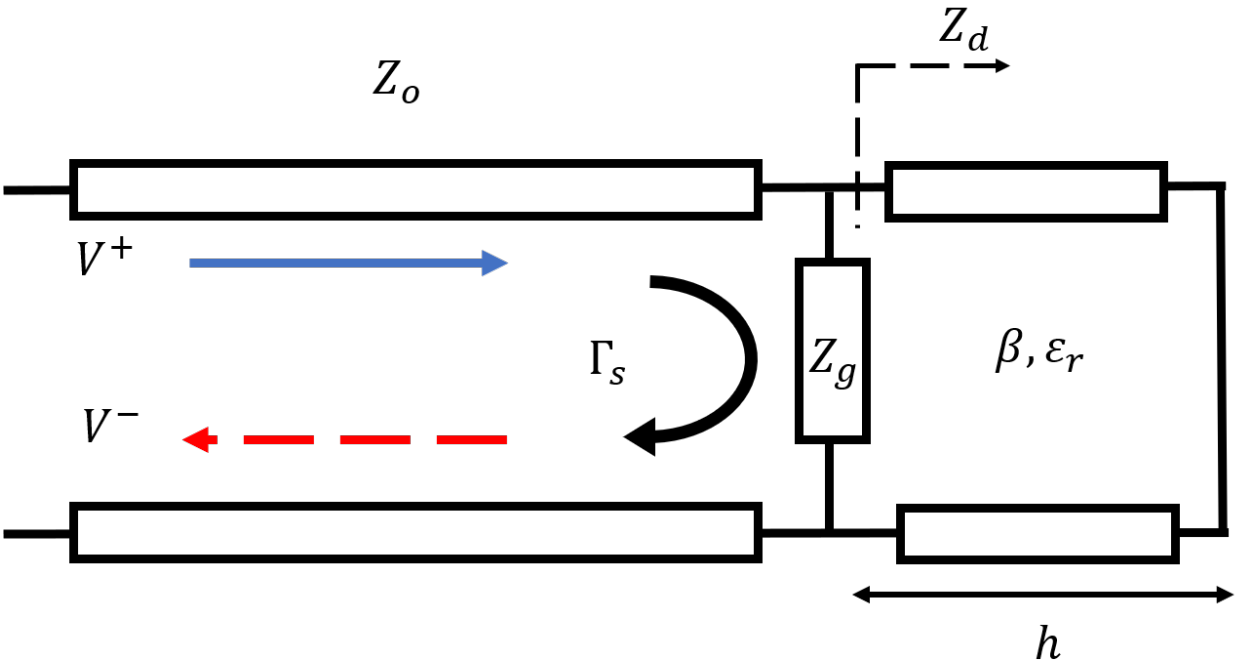

Figure 2.2: Transmission line model for metasurface of metal patches/strips on top of metal backed dielectric slab with thickness h.

$$\frac{1}{Z_s^{TE}} = \frac{1}{Z_g^{TE}} + \frac{1}{Z_d^{TE}} \tag{2.3}$$

$$\frac{1}{Z_s^{TM}} = \frac{1}{Z_g^{TM}} + \frac{1}{Z_d^{TM}} \tag{2.4}$$

where Z_g is the grid impedance on the surface, and Z_d is the impedance by the shorted transmission line of length h. Z_g is related to the shape of the metallization pattern and the dielectric. Z_d is determined by the substrate thickness h and the wave propagation constant β in this corresponding dielectric.

The reflection coefficient can be calculated:

$$\Gamma_s^{TE} = \frac{Z_s^{TE} - Z_0^{TE}}{Z_s^{TE} + Z_0^{TE}} \tag{2.5}$$

$$\Gamma_s^{TM} = \frac{Z_s^{TM} - Z_0^{TM}}{Z_s^{TM} + Z_0^{TM}} \tag{2.6}$$

Aside from this direct calculation based on the geometry of elements, one can easily extract the reflection coefficients for TE and TM from full wave simulation tools. This will be discussed in the next section. With reflection coefficient, reflected wave can be expressed by:

$$V^- = \Gamma_s V^+ \tag{2.7}$$

In general, the reflection coefficient is a complex number. But if the magnitude of the reflection coefficient of the chosen elements is close to unity, those basic elements can be characterized only by their phase response. The scattered field pattern can be calculated by the 2D array model. First, when the incident wave impinges on the board, there will be different phase excited at different locations due to the wave front. The wave will be re-radiated from different elements with local phase response. We can assume the phase response (either TE or TM) of element (p, q) is ψ_{pq}, where p denotes the element position in x-dimension (physical position as x=pd, $p = 1, \cdots, N$) and q denotes the element position in y-dimension (physical position as y=qd, $q = 1, \cdots, M$). The scattered field pattern can be represented by superposition of the initial excitation phase and phase response of each element:

$$U(\theta_r) = \sum_{p=1}^{N} [e^{jkpdsin(\theta_i)} e^{jkpdsin(\theta_r)} \sum_{q=1}^{M} e^{j\psi_{pq}}] \tag{2.8}$$

In this equation, k is the wave number in free space, and $kpdsin(\theta_i)$ is the excitation phase related with the location of element. Note that the elements inside one group cell will have same phase response. This is a general scattered pattern equation for all possible phase response with given polarization. To achieve the desired retroreflection pattern, ψ_{pq} should be determined at each location. In this process, we use genetic algorithm [47],[48] to optimize the distribution of the phase on the surface for the desired application. It has been used in

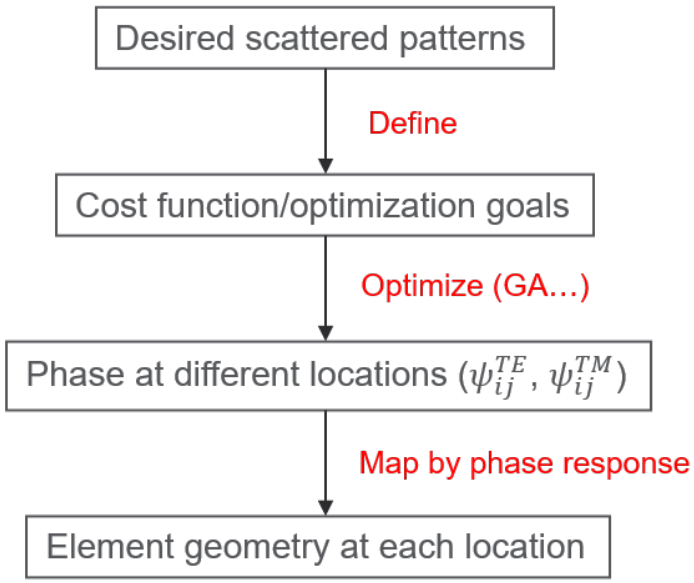

Figure 2.3: Design procedures of nonperiodic metasurface.

the past to tailor the radiation pattern of phased array antennas [49, 50]. Once the phase response at different locations are determined, we can map the phase to real elements with corresponding geometry. For TE/TM and circularly polarized wave, this mapping process requires different sets of basic elements for desired phase response. The design procedure is summarized in Fig. 2.3.

Note that the theoretical pattern calculation process resembles that used in phased array antenna, where each antenna element will be fed with given phase. But the elements in this nonperiodic metasurface design are purely passive and will only re-radiate the wave. The phase response of each element is not guaranteed by the feeding system but instead by its geometry shape with locally periodic boundary condition.

CHAPTER 3

Nonperiodic Metasurface for Retroreflection of the Plane Wave

3.1 Retroreflection of TE/TM Wave

In this case, we will design a nonperiodic metasurface that can retroreflect TE and TM wave simultaneously. From the previous theory, the design will start from the basic elements that can provide a set of TE phase response (ψ_{ij}^{TE}) and a set of TM phase response (ψ_{ij}^{TM}). Then elements at different locations are optimized to achieve a retroreflection pattern.

3.1.1 Design of Basic Element

The design of basic element plays a crucial role in the construction of the nonperiodic metasurface. First, the magnitude of reflection coefficient should be equal or close to unity under oblique TE/TM incidence, so that the element can be characterized by its phase response and pattern equation (2.8) is valid. Second, such basic element configuration is supposed to provide wide phase response for both TE and TM when changing the geometry. This will prepare a large set of available elements to support the optimization process. In addition, the fabrication should be as easy as possible with little error to eliminate the swing of phase response that may interrupt the pattern.

To satisfy all these constraints, one feasible element configuration is square metal patch on top of metal backed substrate as shown in Fig. 3.1 [45]. A single square copper patch

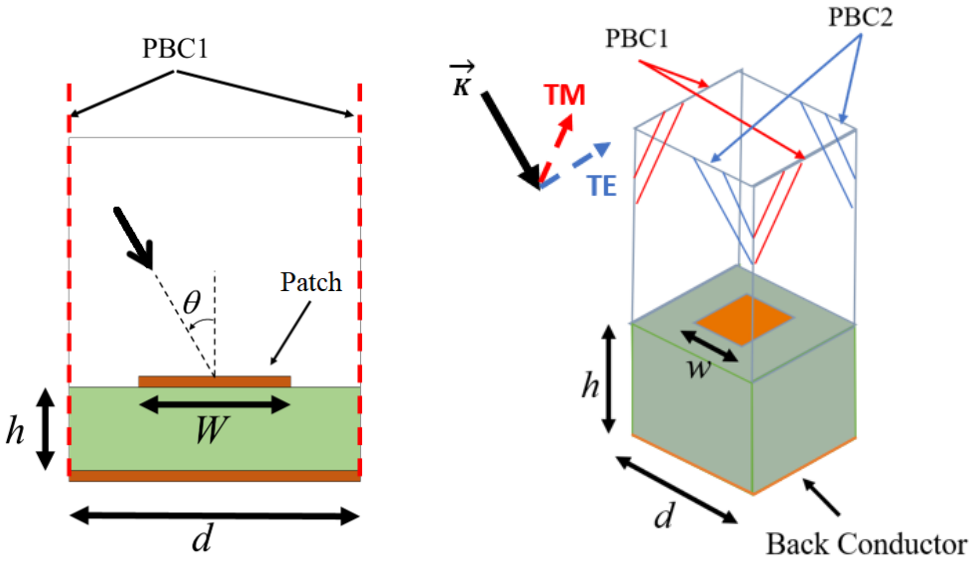

(a) Front view. (b) Perspective view.

Figure 3.1: Schematic of basic element (square patch) for TE/TM incident wave.

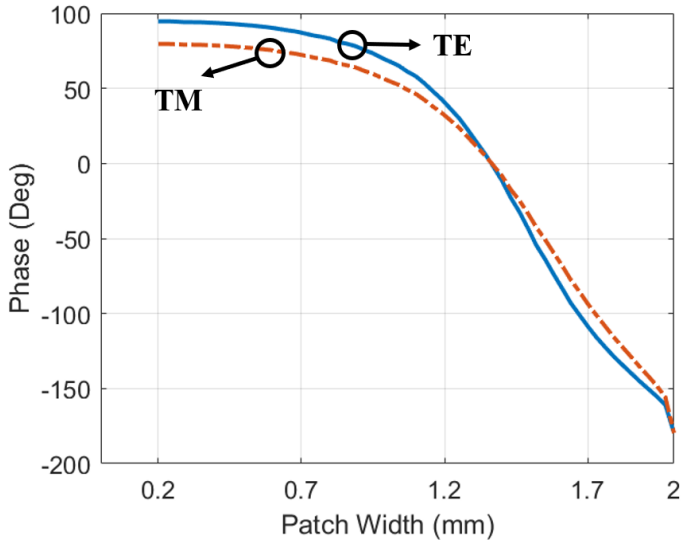

Figure 3.2: TE and TM phase response vs. the top patch width under $-30°$ incident wave at 10 GHz.

with dimension of w is placed on a copper backed Rogers 6010 board with dielectric constant of 10.2 and loss tangent 0.002. The thickness of substrate is 1.91mm. To extract the phase response, periodic boundary condition (PBC) is applied to the four sides of this basic element. The total element size is $d = 2mm$. Floquet port is put on the top to capture the reflection coefficient for both TE and TM oblique incidence. Fig. 3.2 shows the phase of reflection coefficient for TE/TM polarized wave at 10 GHz. As the patch size changes from $0.2mm$ to $2mm$, the phase response for TE and TM range between $+100°$ to $-180°$. The $-180°$ phase response corresponds to the case where the top is covered by metal completely, and therefore the whole surface resembles PEC (perfect electric conductor). The minimum geometry of patch is $0.2mm$ considering the fabrication resolution. Additionally, we simulate the element with no top metallization, giving us $+100°$ for TE and $+85°$ for TM. This blank element will later be automatically placed at the board edge to reduce possible edge effect. All those reflection coefficients are very close to 1 (larger than 0.99) in magnitude, and this will guarantee the element can be characterized solely by its phase response. They will become available elements in the optimization database, where proper elements will be assigned for every location on the surface by optimization.

3.1.2 Theoretical and Simulation Results

Knowing that the reflected beam tends to appear in the specular direction as in some conventional metasurface gratings, our design objective is to enhance the retroreflection beam ($\theta_r = -30°$) and suppress the specular beam ($\theta_r = +30°$).

Therefore, a practical cost function for the operating genetic algorithm can be set as:

$$F = \frac{\max\{\underset{\theta_r \in \{\text{side lobe angles}\}}{\quad |U(\theta_r)|^2 \quad}, \underset{\theta_r \in (+20°, +50°)}{1.5|U(\theta_r)|^2}\}}{\max\{\underset{\theta_r \in (-40°, -20°)}{|U(\theta_r)|^2}\}} \tag{3.1}$$

where $\{\text{side lobe angles}\} = (-90°, -40°) \cup (-20°, +20°) \cup (+50°, +90°)$.

The denominator means the peak of the retroreflection beam and the numerator finds

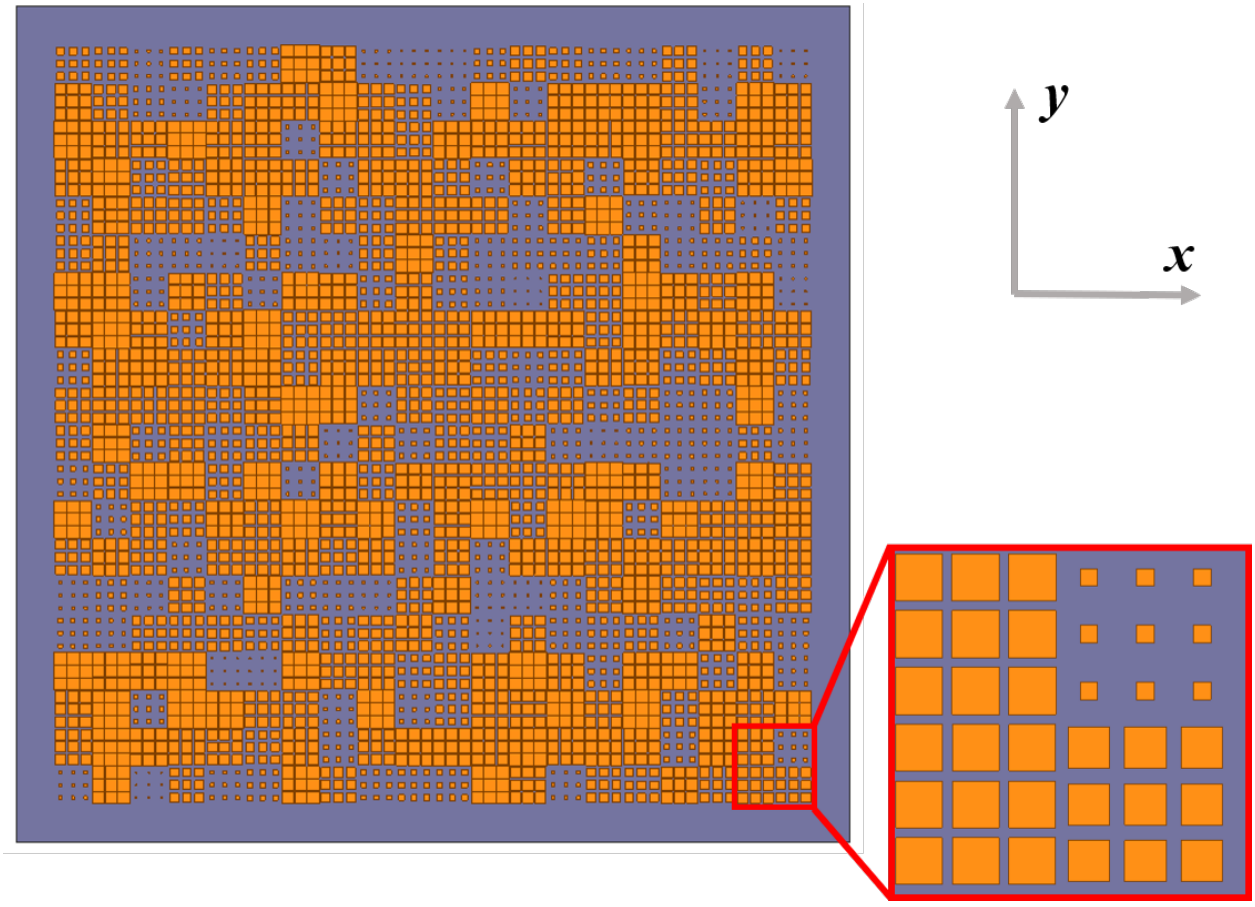

Figure 3.3: Top view of nonperiodic metasurface for retroreflection of TE/TM wave. Purple indicates the substrate and orange indicates top metallization.

the largest value of the side lobes with extra weight applied around the specular direction $\theta_r \in (+20°, +50°)$. In the process of minimizing the cost function by genetic algorithm, the retroreflection $\theta_r \in (-40°, -20°)$ will be enhanced, while the side lobe levels will be reduced and particularly the specular scattered power will be suppressed with additional weight.

In this design, each group cell contains 3×3 basic elements, and there are in total 20×20 group cells on the metasurface. Inside group cell, each element is characterized by its TE/TM phase pair (ψ_{ij}^{TE},ψ_{ij}^{TM}) associated with the patch width w_{ij}. The TE and TM scattered patterns of $\theta_i = -30°$ incidence are constructed every generation based on equation (2.8). Since TE and TM patterns are different, the multiple of their cost functions (3.1) is evaluated to optimize both patterns simultaneously. The range of the available phase values will be considered in the optimization. Then according to Fig. 3.2, all the optimized phase response will be mapped to the elements with corresponding patch size at each location.

Fig. 3.3 shows the top view of the nonperiodic metasurface obtained from the optimization. The entire board is 13.2cm by 13.2cm with 3600 non-blank elements. The purple represents the substrate and the orange represents the top metal patches that distribute in a nonperiodic fashion. Note that the edge of the board is forced to have no metallization to reduce possible edge effect, which may contribute to the unwanted artifacts in the scattered power pattern. The phase of these blank elements at the edge will also be considered in the calculation of scattered power pattern, meaning (ψ_{ij}^{TE},ψ_{ij}^{TM}) at the board edge are forced to be (+100°,+85°).

Such nonperiodic metasurface is simulated in HFSS under $-30°$ TE and TM incidence respectively. Their simulated patterns are overlaid with theoretical patterns in Fig. 3.4 and Fig. 3.5. The theoretical patterns are derived from pattern equation (2.8) with optimized element phase response. Both sets of patterns are normalized to their maximum power.

From Fig. 3.4 for TE polarization, both theoretical pattern and simulation pattern clearly show a main beam at the scattered angle of $-30°$. In the theoretical pattern, the side lobes including those around specular angle (+30°) are suppressed under -7 dB, which complies

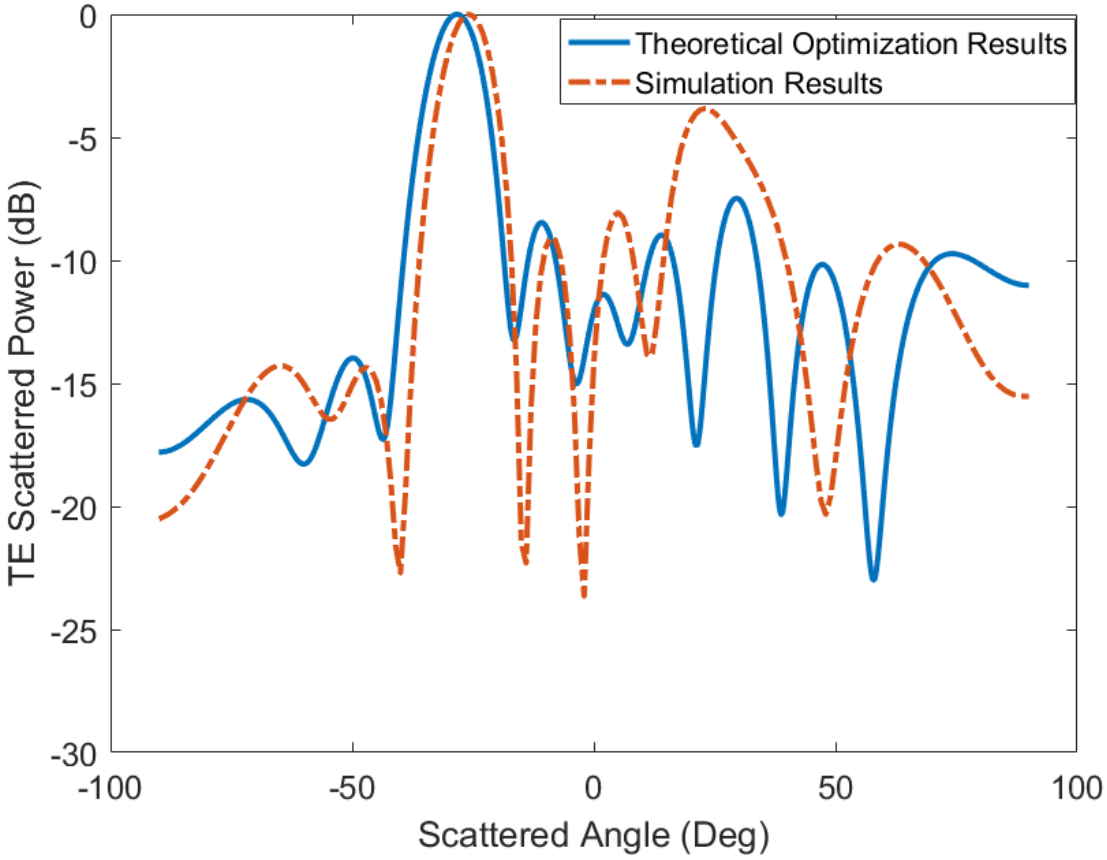

Figure 3.4: Scattered pattern of nonperiodic metasurface for retroreflection under -30° inicdence of TE wave. (solid curve:theoretical pattern; dashed curve: simulation pattern.)

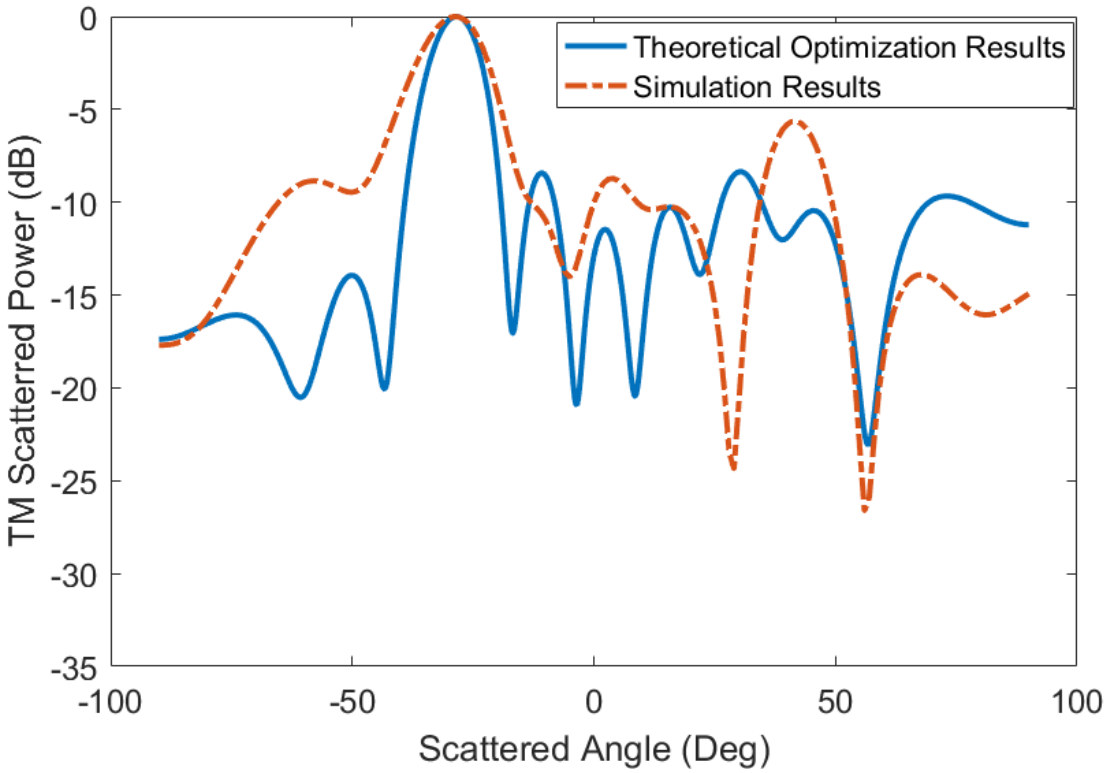

Figure 3.5: Scattered pattern of nonperiodic metasurface for retroreflection under $-30°$ inicdence of TM wave. (solid curve:theoretical pattern; dashed curve: simulation pattern.)

with the cost function (3.1) well. The full wave simulation pattern in general follows the same trend as in theoretical pattern with little elevation in the specular direction and a $+2^\circ$ shift of the main beam. The highest side lobe of simulation pattern appears at $\theta_r = +23^\circ$ of amplitude 3.83 dB lower than the main beam. The major features are well preserved. Compared to the TE-only metagratings proposed in [29] with relatively -2.4 dB specular lobe level, the specular reflection is well suppressed.

The theoretical TM scattered pattern depicted in Fig. 3.5 has almost the same shape as the TE pattern because they share the same cost function. The main features of TM simulation pattern again match those of the theoretical pattern, despite the slightly broadened main beam and highest side lobe shifted to 45° with amplitude 5.65 dB than the main beam.

These small discrepancies between the theoretical and simulation patterns mainly result from the simplified array model based on element phase response without physical constraints such as finite aperture size and material properties. The complete scattering behavior can be studied based on classical formation of electromagnetic theory (e.g. Maxwell's equations). For example, in our model we assume isotropic element pattern regardless of the element shape, based on the low radiation directivity of small aperture size ($1/15\lambda_0$) in antenna theory. In fact, the pattern of every element will be slightly different from the isotropic pattern and this error will accumulate when it comes to modeling a metasurface with 3600 elements. Similarly, the swing of element reflection magnitude from 0.99 to 1 will also contribute to the pattern mismatch. In addition, the edge effect is not considered in the model, since the periodic boundary condition of the elements near the board edge will be no longer valid. Although in our design, we force the optimized elements to be located away from the board margin and compensate the edge scattering with the phase of blank elements (with $+100^\circ$ TE phase and $+85^\circ$ TM phase), this edge effect will still not be eliminated. The elements located at the corners or edges of the group cells may experience the same inaccuracy problems, because they also neighbor elements from other group cells and the periodic boundary condition will not be strictly observed. Nevertheless, when a

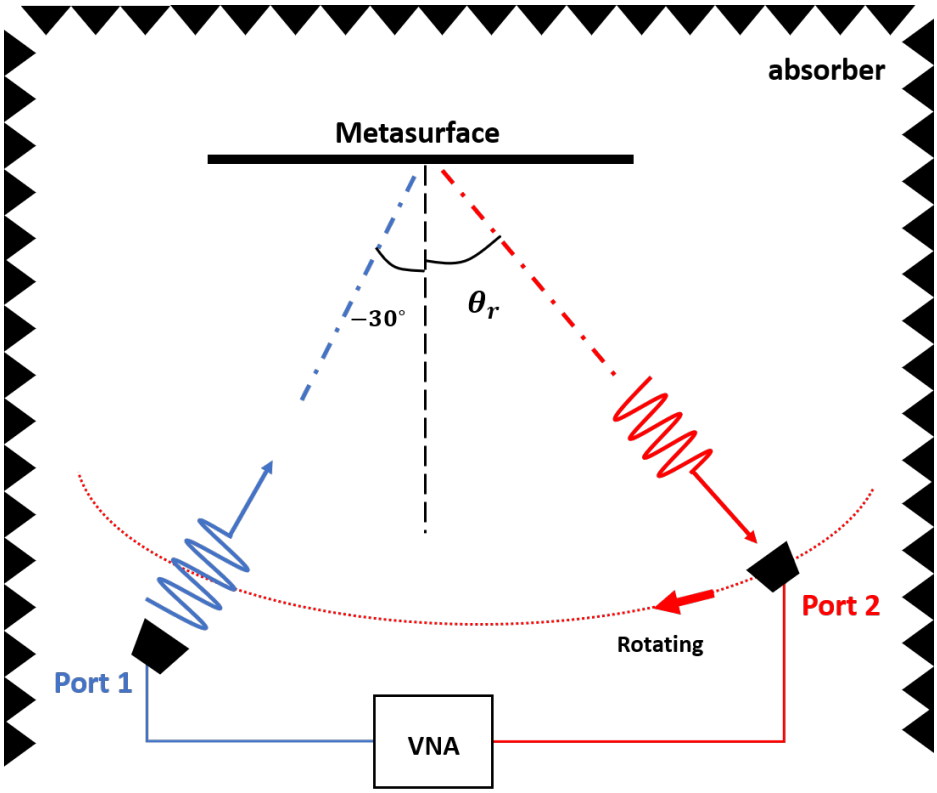

Figure 3.6: Two-port measurement setup for scattered power pattern of nonperiodic metasurface for TE/TM retroreflection. (blue: incident wave; red: scattering wave)

large number of elements are used to make up the metasurface, the scattering behavior will still be dominated by the array model with elements' phase response. As a result, in our metasurface with 3600 elements, main features of theoretical patterns and simulation patterns match well.

3.1.3 Measurement Result

This nonperiodic metasurface is fabricated using Rogers RT/duroid 6010 laminate by LKPF ProtoLaser U4. Fig. 3.6 shows the experimental setup for measuring the scattered power pattern under oblique incidence. Similar to the bistatic RCS measurement, two horn antennas are connected to the two ports of VNA acting as a transmitter (port 1) and a receiver

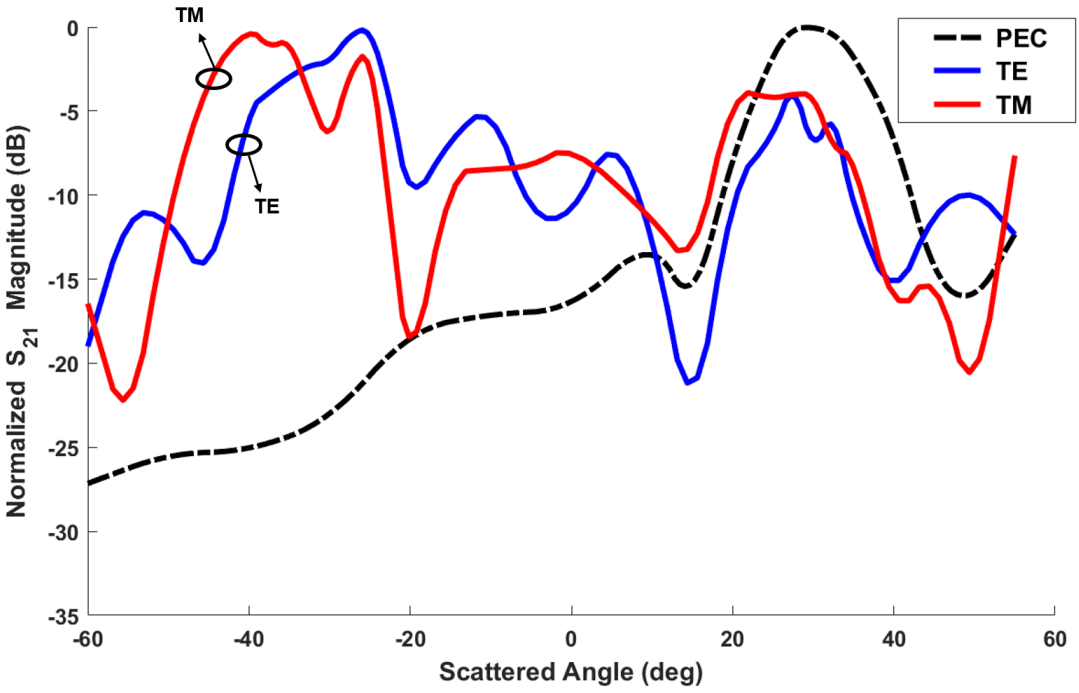

Figure 3.7: Measured far field scattered power patterns of PEC (dashed black), nonperiodic metasurface under TE incidence (solid blue) and TM incidence (solid red).

(port 2). The metasurface is placed at the far zone of the antennas with $\theta_i = -30°$ to the transmitter. Reveiver antenna can be rotated to measure S_{21} at different scattered angles. Surroundings of this setup are covered with absorbers to prevent environment scattering.

Fig. 3.7 shows the normalized measured scattered power under $-30°$ TE and TM incident wave. For calibration, a piece of metal board (PEC) with the same size is also measured in the same environment, and the scattered pattern is depicted as the dashed curve. The main beam is at specular direction ($\theta_r = +30°$), following the law of reflection on PEC. However, both the measured TE and TM patterns of metasurface show the main beams at around $\theta_r = -30°$ direction, indicating its retroreflection property for TE/TM polarization. The main features and the trend of the pattern match well with the theoretical and simulation patterns. The largest side lobes of TE pattern is 3.91 dB lower than the main beam and the largest side lobe of TM pattern is 3.50 dB than the main beam, which is predicted in our

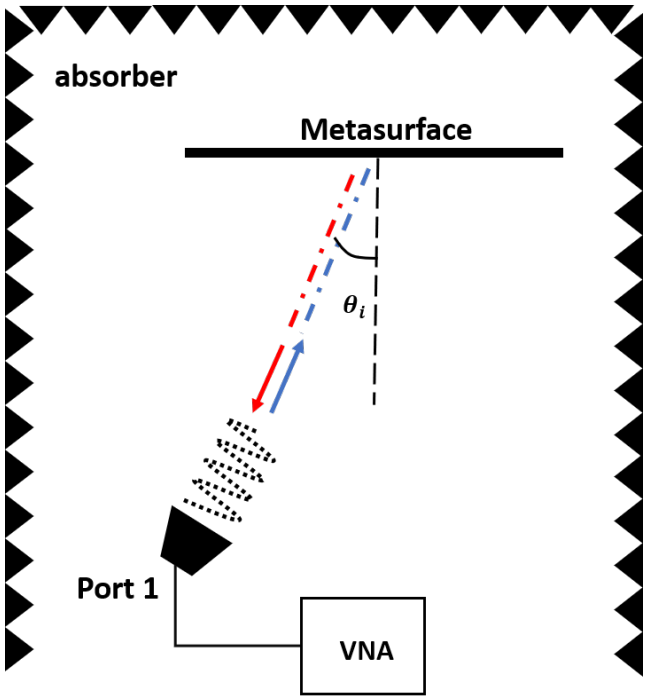

Figure 3.8: One-port measurement setup for retroreflection of metasurface.

optimization goal. The main beam of TE pattern is broadened to some extent compared to the simulation pattern and theoretical pattern. For TM measured pattern, there exists a dip in the main beam and specular scattering is slightly stronger than simulation.

These discrepancies are in part due to the measurement setup. When rotating receiver antenna to retroreflection angle $\theta_r = -30°$, port 2 receiver will be placed between port 1 transmitter and the board under test. Therefore, it will block some of the incidence power from reaching the board compared to other angles. The measured S_{21} at the retroreflection direction is lower than expected and will cause a dip or the expansion of the main beam. The specular power will become relatively stronger. However, the PEC scattered pattern is barely affected because the strong specular power is not blocked in this setup. Despite all these factors that may raise the specular level, this result is still better than that in [29] where 2.4 dB relative specular power level is measured.

To calibrate the absolute retroreflection power, we set up a one-port measurement shown

in Fig. 3.8. The horn antenna is connected to port 1 of VNA and will illuminate incident wave to the board as well as receive the retroreflected power. Compared to the two-port measurement in Fig. 3.6, this setup is simpler and can detect the absolute retroreflected power without blockage due to the port alignment. It is known that PEC is an ideal retroreflector for normal incidence and a copper board of the same size should be a good reference with high retroreflected power. The normal retroreflection (port 1 at $\theta_i = 0°$) of copper board is measured as $S_{11} = -39.3$ dB, whereas the metasurface TE and TM retroreflection power levels (port 1 at $\theta_i = -30°$) are 0.9 dB and 1.5 dB lower respectively. Note that the metasurface of oblique incidence will have inherently smaller effective aperture size than the PEC of normal incidence, which contributes to 0.62 dB lower in power for $\theta_i = -30°$. Other retroreflection degradation may come from the dielectric and conduction loss of metasurface as well as wider retroreflection beam than copper board. Nonetheless, this measurement of metasurface shows strong retroreflection property which is still comparable to its copper counterpart.

3.2 Retroreflection of CP Wave with Reversed Handedness

Circularly polarized wave has been extensively used in satellite communication [51] and optical communication [52], due to its high link reliability and resistant to Faraday effect. However, retroreflection of circularly polarized wave has rarely been investigated due to the difficulty in manipulating correlation of TE and TM phase. The method used in the previous section works for TE/TM polarization, but the square patch elements cannot guarantee the TE and TM phase to remain 90° difference after reflection-i.e., in the case where the incident wave is circularly polarized, TE and TM components will be retroreflected differently and no longer form a CP wave. To overcome this limitation, we will present an element configuration based on rectangular patch with equal TE and TM phase response [42]. Since the wave vector is reversed after reflection, the handedness of CP wave will also be reversed by this type of

Table 3.1: TE/TM phase response vs. rectangular patch size w_x and w_y

w_x(mm)	w_y(mm)	TE/TM phase	w_x(mm)	w_y(mm)	TE/TM phase
1.20	0.42	$+81.52°$	1.45	1.47	$-11.33°$
1.20	0.94	$+63.87°$	1.5	1.53	$-30.11°$
1.25	0.31	$+83.01°$	1.55	1.60	$-49.56°$
1.25	1.09	$+51.87°$	1.6	1.66	$-68.46°$
1.30	1.20	$+39.98°$	1.65	1.72	$-85.72°$
1.35	1.30	$+24.27°$	1.7	1.77	$-100.83°$
1.4	1.39	$+7.45°$	1.75	1.82	$-114.18°$

metasurface.

3.2.1 Design of Basic Element

Fig. 3.9 shows the schematic of the basic element for CP wave. A rectangular metal patch with dimension of w_x by w_y is placed on the metal backed substrate. Other parameter notations are the same as Fig. 3.1. Periodic boundary condition is applied at four sides of the element and Floquet port is put on the top to extract the phase response for TE/TM oblique incidence. We find in the simulation that the response of TE is determined by w_y, because TE wave is mainly affected by the interval between the metal in y- dimension of the board. Similarly, the response of TM mainly depends on the dimension of w_x. From the parametric study of w_x and w_y, we find a list of elements with equal TE and TM phase response shown in Table 3.1. The rectangular patch can achieve a relatively large range of phase response from $+81.52°$ to $-114.18°$ when varying w_x and w_y from 0.2mm to 2mm at 10 GHz. In addition, the magnitude response of all the listed elements is close to 1 (all larger than 0.99) to guarantee that the elements can be characterized by their phase. The listed 14 elements will become available elements in the optimization database to be assigned at different locations on the metasurface.

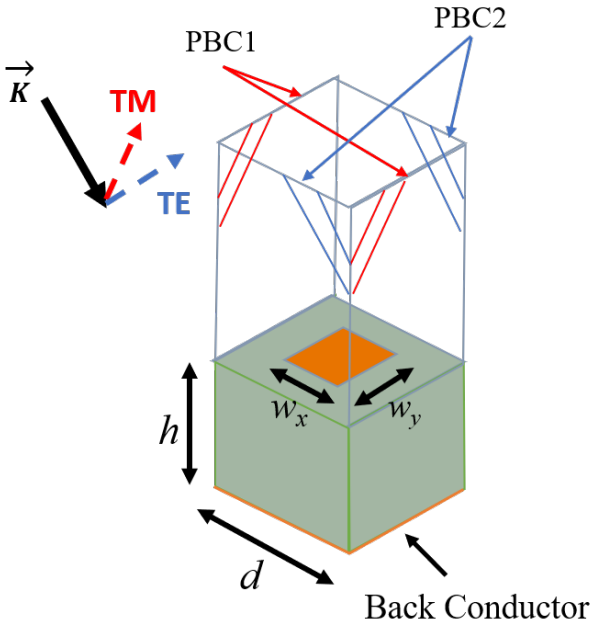

Figure 3.9: Schematic basic element (rectangular patch) for circularly polarized incident wave.

3.2.2 Theoretical and Simulation Results

The scattered pattern of CP wave under $\theta_i = -30°$ incidence can be constructed by equation (2.8) and optimized each generation by cost function (3.1). The optimized phase at each location is then mapped by the relation shown in Table 3.1.

Fig. 3.10 shows the top view of such nonperiodic metasurface under left-hand circularly polarized (LHCP) incident wave. In this design, each group cell has a cluster of 4×4 identical elements. The whole metasurface is 12cm by 12cm in size that contains 225 group cells (3600 basic elements). Because of the handedness reversal property of this metasurface, we will investigate the far field pattern of scattered right-hand circularly polarized (RHCP) wave.

Fig. 3.11 shows the HFSS full wave simulation pattern and theoretical optimized pattern derived from equation (2.8) at 10 GHz, both normalized by their maximum power. From the figure, the main beams of the simulation pattern and theoretical pattern are located

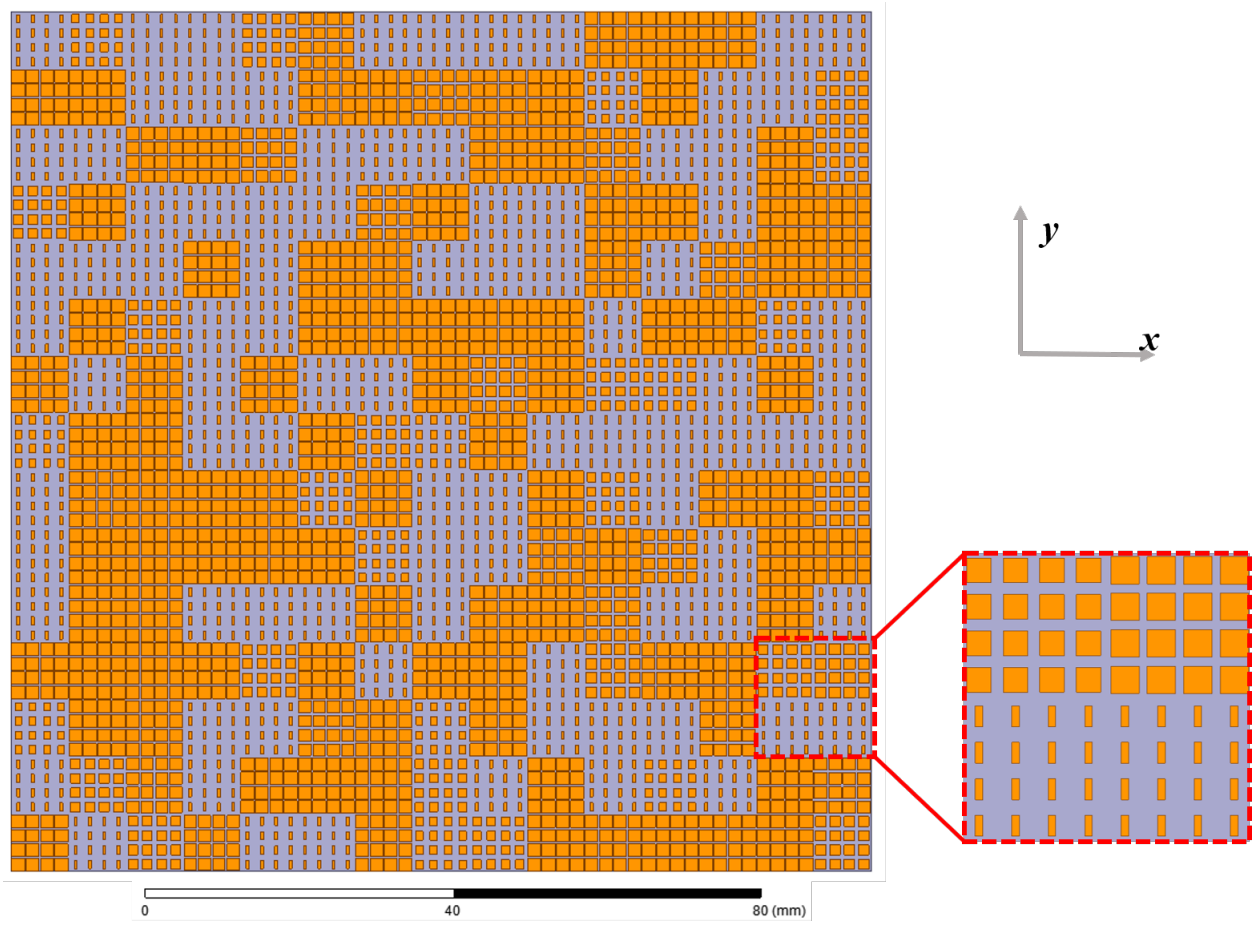

Figure 3.10: Top view of nonperiodic metasurface for retroreflection of CP wave with reversed handedness.

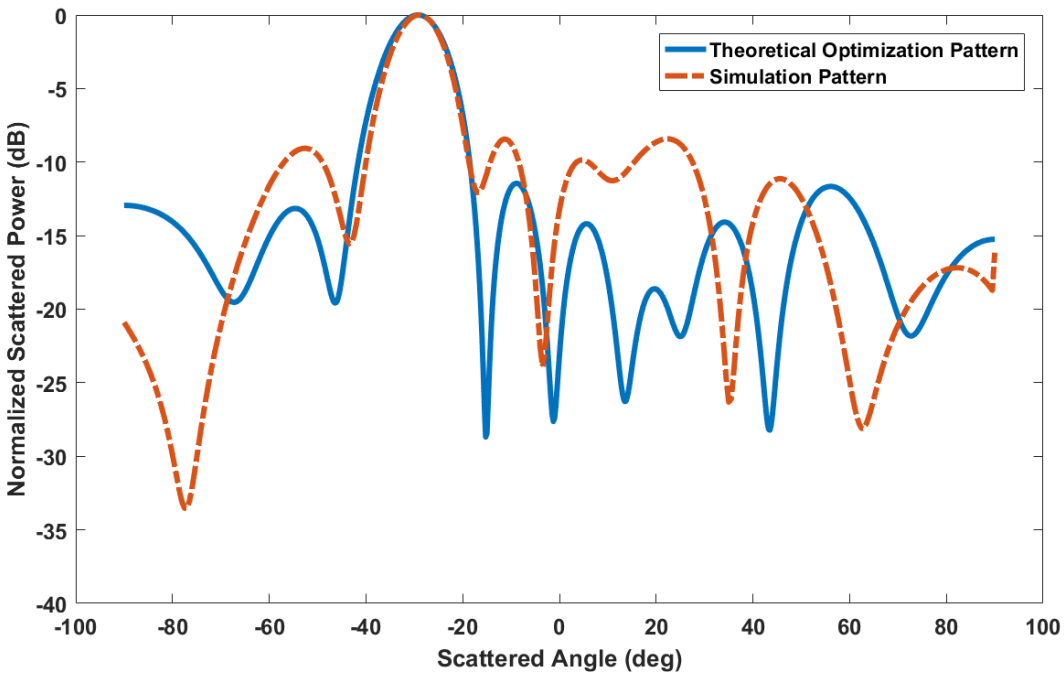

Figure 3.11: Theoretical optimized scattered pattern (solid curve) and simulation pattern (dashed curve) of nonperiodic metasurface for CP retroreflection with reversed handedness.

at $\theta_r = -30°$ indicating the retroreflection of CP wave. Besides, major features of both patterns such as beamwidth match well with each other. For theoretical pattern, all the side lobes are lower than -10 dB and the scattered power at specular direction is below -12dB due to the extra weight applied to the corresponding region in the cost function. The simulation pattern follows the same trend as the theoretical pattern, with a little elevation of side lobes, the highest of which is around -8.5 dB. Similar to the TE/TM design case, these small discrepancies may result from the simplified scattered power pattern model with assumption of isotropic element pattern, swing of the element reflection magnitude and the inaccurate phase of elements at the edge of the board or group cells.

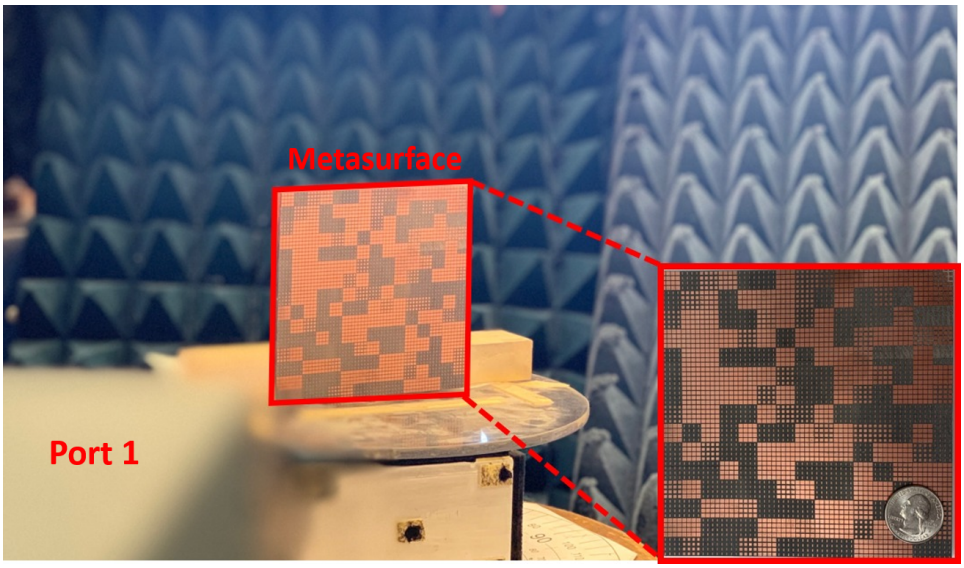

Figure 3.12: Measurement setup for retroreflection of oblique CP incident wave on the nonperiodic metasurface.

3.2.3 Measurement Result

This metasurface shown in Fig. 3.10 is fabricated and its retroreflection of CP wave is measured by the one-port experimental setup of Fig. 3.8 (real setup and fabricated board shown in Fig. 3.12). Again, to calibrate the path loss and environment scattering, S_{11} of a piece of copper board (PEC) with the same size is measured at $\theta_i = 0°$. The copper is known to have strong retroreflection for normal incident wave and will also reverse the handedness of the CP wave.

Note that we do not directly use one CP horn to perform the measurement because it is unable to receive the reflected wave with reversed handedness. Instead, we still use rectangular horn to transmit and receive TE and TM polarized wave respectively. Then we use the TE/TM retroreflection with both magnitude and phase to synthesize the corresponding scattered field under LHCP incidence. The received total field can be separated into LHCP/RHCP components. This method is valid because either TE/TM or LHCP/RHCP is a complete basis for a plane wave.

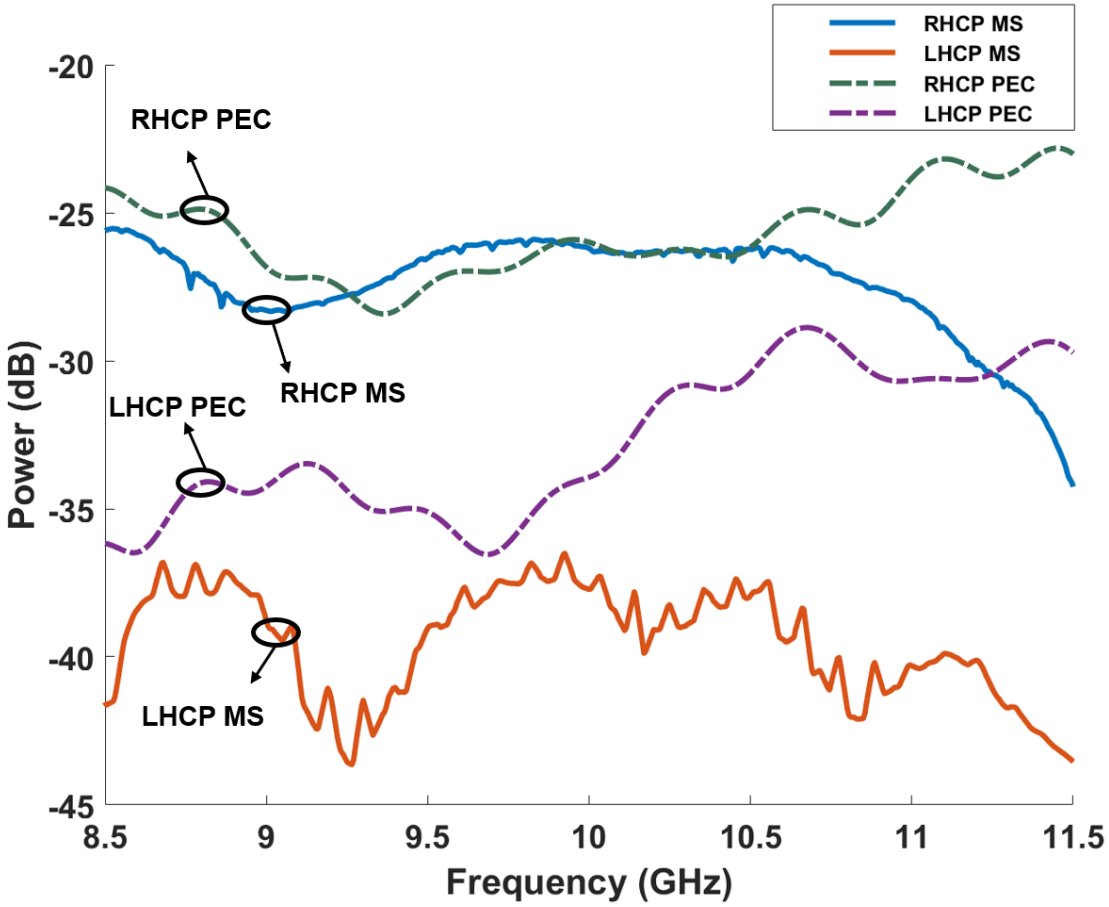

Figure 3.13: Retroreflected RHCP and LHCP power (S_{11}) for metasurface (solid curves) and PEC (dashed curves), under LHCP incidence.

Fig. 3.13 shows the measured result of the nonperiodic metasurface under LHCP incidence. To avoid the measurement setup error, we rotate the board around the designed retroreflection angle ($\theta_i = -30°$), and find the maximum retroreflection power achieved at $\theta_i = -24°$. Besides the experimental alignment error, this small shift of retroreflection angle may result from the slight swing (± 0.25) of the dielectric constant of the Rogers 6010 laminates.

Solid curves in Fig. 3.13 show the retroreflection power (S_{11}) of this metasurface. At 10 GHz, RHCP power is 11.5 dB larger than LHCP power, indicating that the handedness

of LHCP incident wave has been reversed after retroreflection from the metasurface. Two dashed curves show the retroreflection power of PEC board at the same position under normal LHCP incidence, serving as a reference. From Fig. 3.13, the RHCP power of metasurface and PEC is almost at the same level at 10 GHz. At some frequencies points below 10 GHz, RHCP power of metasurface seems to be slightly larger than that of PEC. This synthesizing error may result from the inaccuracy of horn alignment for TE and TM measurement. At 10 GHz the LHCP component of PEC board is lower than its RHCP counterpart as predicted, but not as much as 11.5 dB. This indicates that the proposed nonperiodic metasurface has good polarization isolation for the retroreflected CP wave.

3.3 Retroreflection of CP wave with preserved handedness

The handedness preserved type metasurface can also be conveniently derived with this non-periodic design method. In this section, elements that can provide 180° difference between TE and TM phase response will be used. Since the wave vector after retroreflection will be reversed, the flip of TE and TM phase difference will preserve the handedness of the CP wave.

3.3.1 Design of Basic Element

Because this design requires large phase difference between TE and TM phase response, the feasible basic element should be able to vary its geometry drastically both in x- and y-dimensions. Fig. 3.14 shows the schematic of such basic element. A piece of cross shape metal is placed on the metal backed substrate [53]. Size of this basic element is set to be $d = 3mm$ and the substrate is Rogers 6010 with thickness of $h = 1.91mm$. The width of each metal bar is $w = 0.6mm$. Periodic boundary condition is applied to the four sides of the element and Floquet port is put on the element top to extract the reflection coefficient under $-30°$ TE and TM incidence. In fact, the response of TE wave is mainly determined

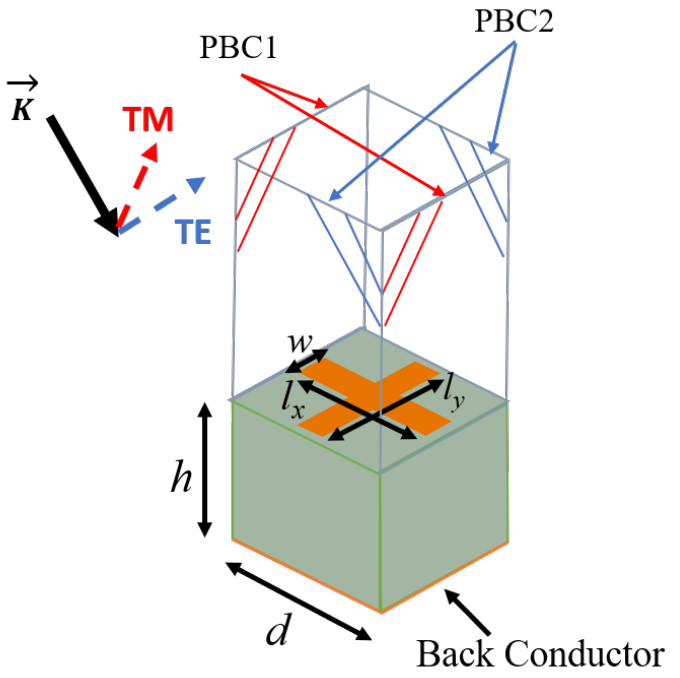

Figure 3.14: Schematic basic element (cross) for circularly polarized incident wave.

by l_y, because the electric field of TE wave is polarized along y-axis, which aligns with the metal bar of length l_y. Similarly, the TM phase response is mainly determined by l_x. Compared to the previous patch shape basic element, this configuration can provide larger phase difference between TE and TM incidence by varying l_x and l_y. To achieve 180° phase difference, feasible elements will either have large l_x with small l_y, or small l_x with large l_y, listed in Table. 3.2.

3.3.2 Theoretical and Simulation Results

Those listed elements will become available in optimization database. Their phase (either TE or TM, since ideally TE and TM theoretical patterns are the same) are used to construct scattered power pattern by equation (2.8) and optimized at different locations against cost function (3.1).

Table 3.2: TE/TM phase response of cross elements

l_x(mm)	l_y(mm)	TE phase	TM phase
1.45	2.90	$-115.8°$	$+64.2°$
2.86	0.80	$+90.6°$	$-89.4°$
2.88	1.10	$+86.8°$	$-93.2°$
2.90	1.30	$+82.7°$	$-97.3°$

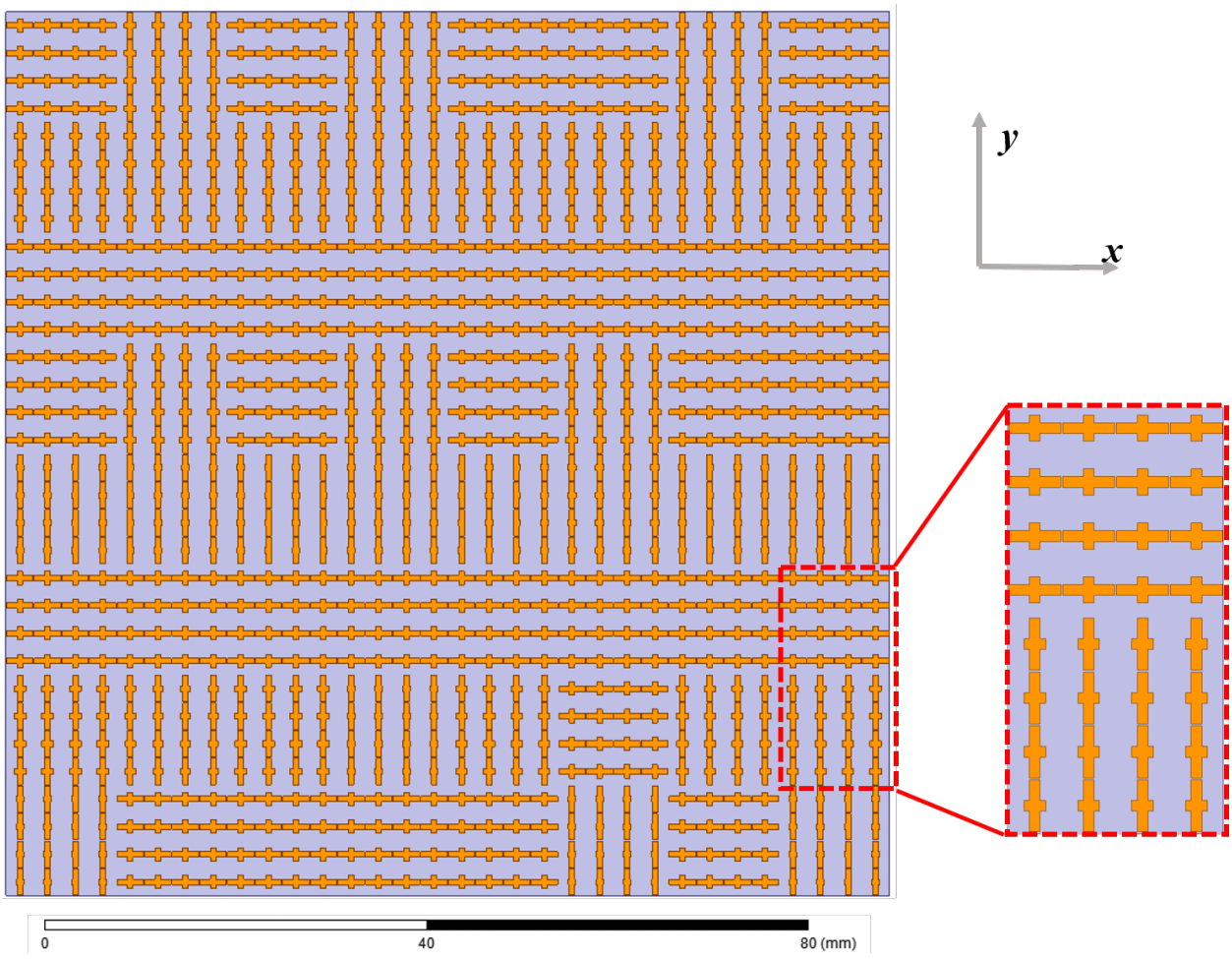

Figure 3.15: Top view of nonperiodic metasurface for retroreflection of CP wave with preserved handedness.

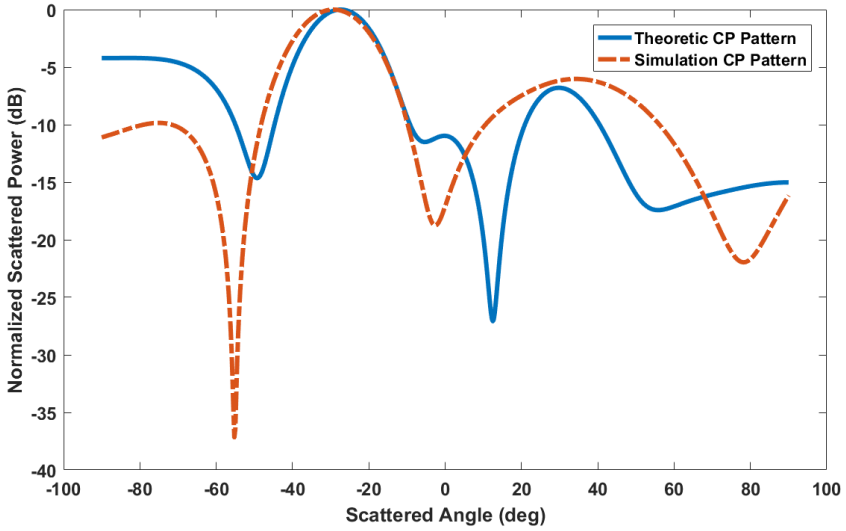

Figure 3.16: Theoretical scattered pattern (solid curve) and simulation pattern (dashed curve) of nonperiodic metasurface for CP retroreflection with preserved handedness.

Fig. 3.15 shows the top view of this nonperiodic metasurface. Orange represents top metallization on the board and purple represents the substrate. Each group cell contains 4×4 basic elements and there are 8×8 group cells across the board. Size of the board is 9.6cm by 9.6cm.

The theoretical pattern derived from equation (2.8) and the simulated scattered LHCP pattern by HFSS are depicted in Fig. 3.16. Features of both patterns match well with each other, with main beams at $-30°$, showing the retroreflection of LHCP incidence with preserved handedness. Side lobes around $+30°$ are below -6 dB, indicating good retroreflection efficiency achieved by applying extra weight of specular direction in the cost function. In the simulation result, the main beam is broadened to a small extent and the scattering in the large angles (toward $\pm 90°$) is lower. As discussed in the previous sections, these discrepancies are inherent to our simplified model that may not predict the complete physical effects. Factors including the basic element pattern error, reflection magnitude error and phase approximation of elements at the edge of the board and the group cells will all cause

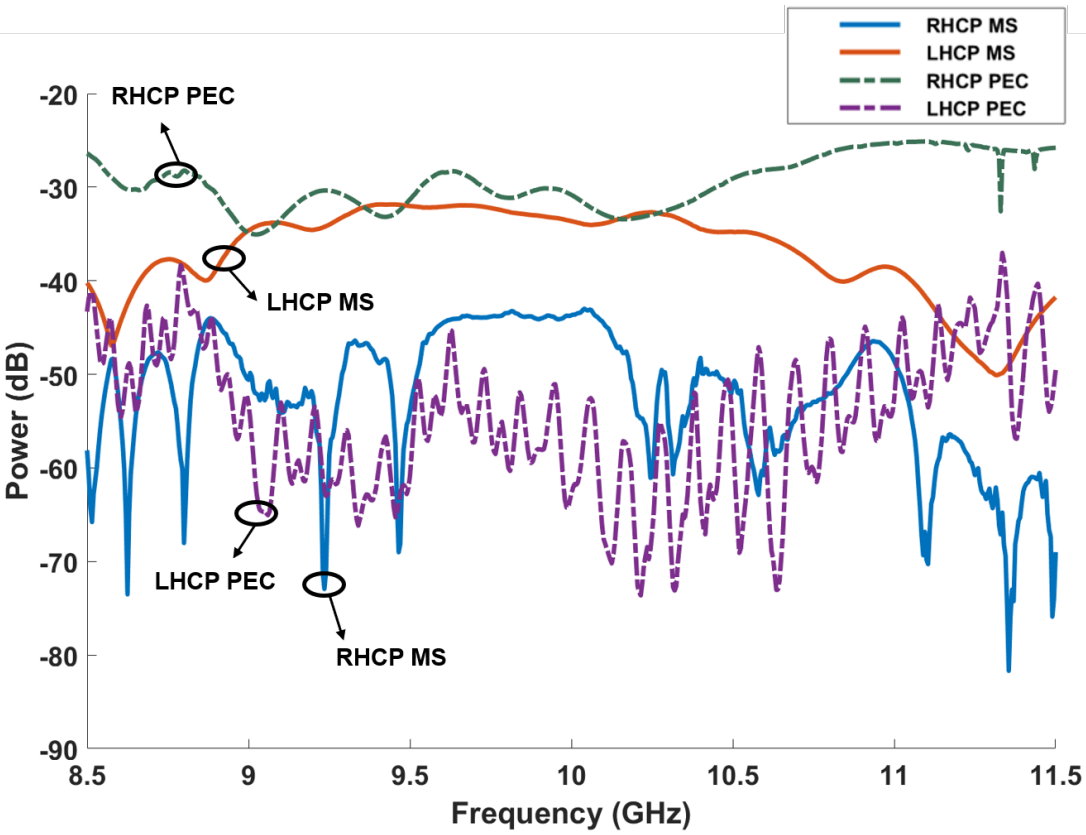

Figure 3.17: Retroreflected RHCP and LHCP power (S_{11}) for metasurface (solid curves) and PEC (dashed curves), under LHCP incidence.

the mismatch of simulation pattern and its theoretical prediction.

3.3.3 Measurement Result

This nonperiodic metasurface is fabricated and measured in the same one-port experimental setup in Fig. 3.8. The metasurface is placed at the far field of port 1 in the angle of $-30°$. Again, a piece of copper board (PEC) with the same size works as a reference and TE/TM retroreflection is used to synthesize the scattered CP power under LHCP incidence.

Fig. 3.17 shows the retroreflected RHCP and LHCP power of metasurface (solid curves) and PEC board (dashed curves). It can be observed that strong LHCP retroreflected wave

from metasurface is detected at 10 GHz, with 10 dB higher in magnitude than its RHCP counterpart. This reflected LHCP power is almost at the same level of the PEC retroreflected RHCP power. This indicates that most of the CP wave is scattered back by this metasurface while preserving its handedness.

CHAPTER 4

Nonperiodic Metasurface Beam Splitter

A beam splitter is a passive device that can split incoming electromagnetic wave into multiple beams. It is widely used in optical devices including interferometers and spectrometers, where the wave is separated into beams with a certain power ratio or separated by its frequency spectrum. Although beam splitter can also find its applications in lower frequency such as wireless power transfer, research in microwave regime has seldom been reported. This is due to the methods used in optics are usually based on frustrated total internal refraction, semi-transmitted mirror or birefringence property of the material and most of these will have difficulty in scaling down the frequency.

A multi-beam reflector with low loss and high gain has been achieved in [54]. The multiple reflected beams rely on the beam scan by mechanically tilting the reflectarray and thus cannot exit simultaneously. Besides, the fabrication is hard to be scaled to THz or optical frequency. Recently, with the development of metamaterial and metasurface, people have more powerful tools to manipulate the propagation of electromagnetic waves in a wide frequency range. A metamaterial based beam splitter has been demonstrated at around 7 GHz [55]. It uses metal strips and dielectric to construct a 3D fishnet structure which presents a near-zero refractive index. However, this design will have a bulky profile and thus will not be easy to fabricate compared to planar structures. A transmissive type metasurface with an arbitrary polarization splitting angle has been investigated in X-band [56]. This structure uses a tri-layer metasurface and again will increase the cost and difficulty in fabrication. A frequency selective surface (FSS) type beam splitter has been proposed in [57], which

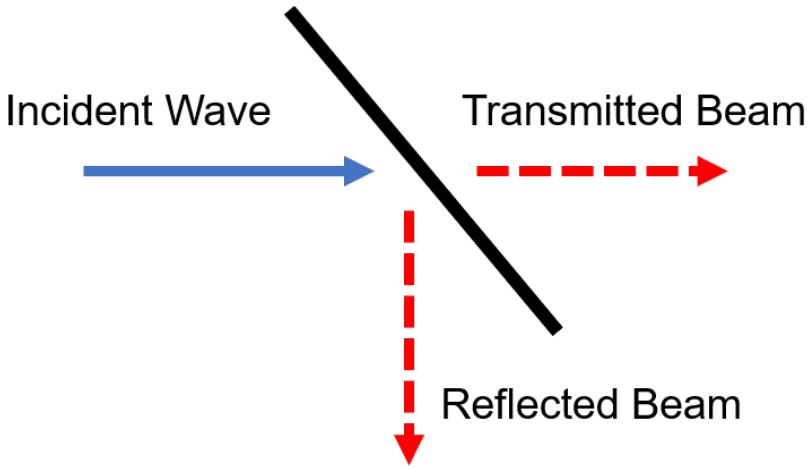

(a)

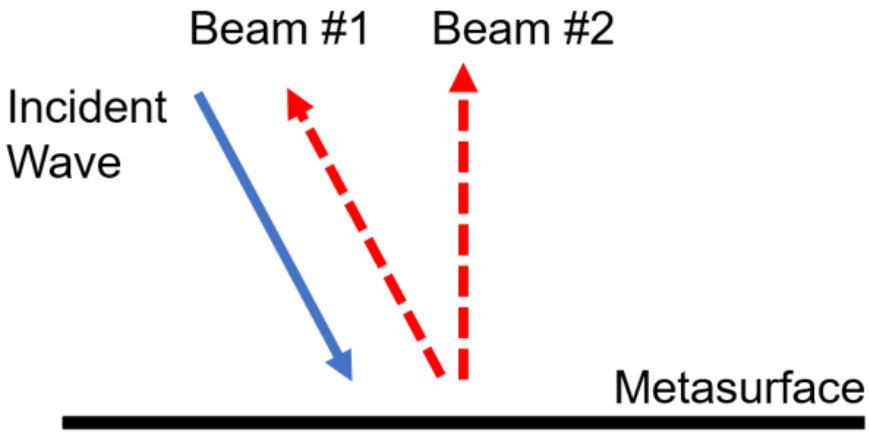

(b)

Figure 4.1: (a) FSS type beam splitter. (b) nonperiodic metasurface type beam splitter. (solid arrow: incidence wave; dashed arrow: splitted beams)

can split an incoming incident wave into a transmitted signal (beam) and a reference signal (beam) with equal power shown in Fig. 4.1(a). Though this method only requires single layer fabrication, it has no control over the angles of the beams; i.e., the transmitted beam is always in the same direction of incidence beam and the reflective beam is always at the specular direction.

In this chapter, we will present a beam splitter based on nonperiodic metasurface. For given oblique incidence plane wave, the metasurface can scatter the wave into two beams at arbitrary designated angles with equal power (or potentially in a designated ratio) as shown in Fig. 4.1 (b). The design of such nonperiodic metasurface follows the procedure dipicted in Fig. 2.3. We first discretize the surface into many subwavelength elements with equal center to center space. Each element will be characterized by its magnitude and phase of reflection coefficient under TE/TM oblique incidence. By properly designing and choosing elements with close to unity reflection magnitude, the scattered pattern with two splitting beams can be obtained and optimized based on array model. In this study, we intentionally set the scattered beams at retroreflection direction and normal direction with equal peak power. An arbitrary board will tend to scatter the beam into specular direction, whereas this metasurface will suppress this intrinsic specular reflection to a very low level. The beam splitting pattern is verified by both full wave simulation and measurement at 10 GHz. Potentially, it enables one to independently control the magnitude of peak power of each beam or change the angles of the beams. Also, the whole design can be conveniently scaled to higher frequencies.

4.1 Design Procedures

We can directly use the same elements proposed in Section 3.1 to build the nonperiodic metasurface to manipulate TE/TM wave. As the patch size changes from $0.2mm$ to $2mm$, the phase response for TE and TM range between $+100^\circ$ to -180°, which is adequate

for the beam splitting application. The TE/TM scattered patterns can be represented by superposition of the initial excitation phase and phase response of each element as in equation (2.8). The optimization goal for the beam splitting patterns can be summarized as:

1. Maximize the scattered power of beam #1 in the retroreflection direction ($-35^\circ < \theta_r < -25^\circ$) and beam #2 in the normal direction ($-5^\circ < \theta_r < +5^\circ$).

2. Equalize the power of beam #1 and beam #2.

3. Minimize side lobes.

4. Minimize scattered power in the specular region ($+20^\circ < \theta_r < +40^\circ$) with extra weight.

Therefore, a practical cost function for the optimization process can be set as:

$$F = \frac{\max\{ \underset{-25^\circ<\theta_r<-5^\circ,+5^\circ<\theta_r<+20^\circ}{|U(\theta_r)|^2}, \underset{+20^\circ<\theta_r<+40^\circ}{1.5|U(\theta_r)|^2} \}}{\max\{ \underset{-35^\circ<\theta_r<-25^\circ}{|U(\theta_r)|^2} \} \cdot \max\{ \underset{-5^\circ<\theta_r<+5^\circ}{|U(\theta_r)|^2} \}} \tag{4.1}$$

where $U(\theta_r)$ is the scattered power pattern defined in equation (2.8). In the optimization process, this cost functions will be minimized. The denominator represents the peak values of two desired beams at retroreflection direction ($-35^\circ < \theta_r < -25^\circ$) and normal direction ($-5^\circ < \theta_r < +5^\circ$). This part will be enhanced. The nominator finds the possible side lobes of other angles and tries to minimize their peak values. The endfire scattering is ignored since intrinsically little power will be scattered into large endfire angles. Also note that additional weight is applied to the specular angles ($+20^\circ < \theta_r < +40^\circ$) to suppress the scattering from that direction.

In the light of those available elements at 10 GHz, we can obtain the scattered pattern of 30° incidence wave with equation (2.8) and use (4.1) to find optimized TE/TM phase values ψ_{pq} at different locations. The phases will then be mapped to the patches with corresponding dimension according to the curves in Fig. 3.2.

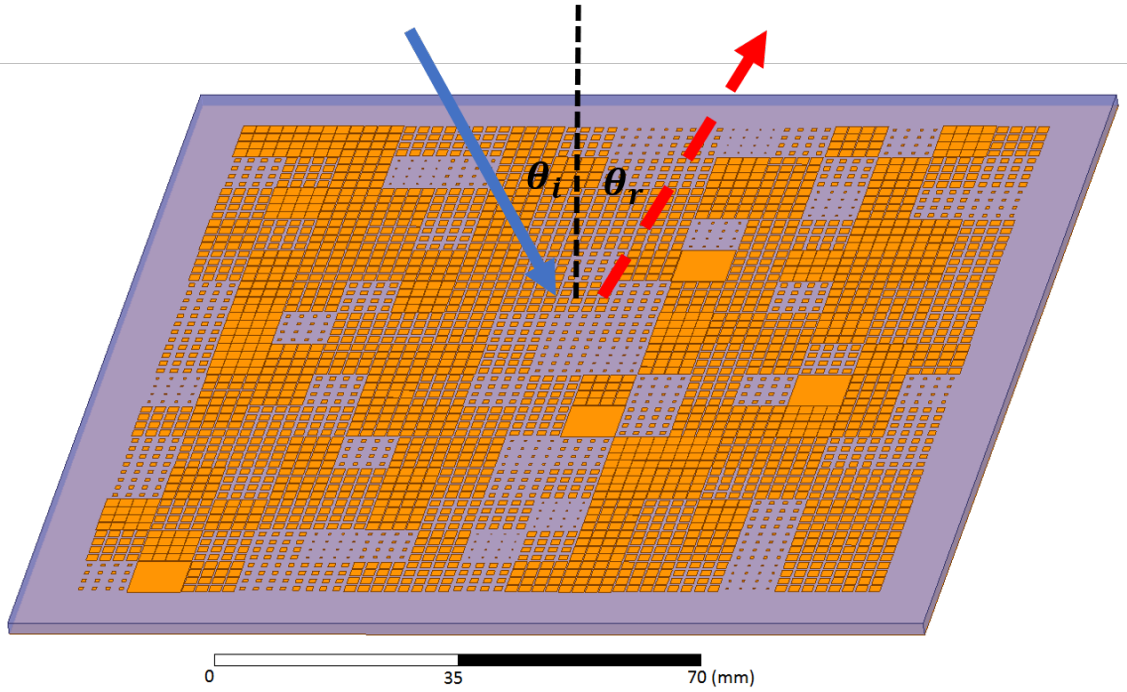

Figure 4.2: Optimized nonperiodic metasurface beam splitter.

4.2 Theoretical and Simulation Results

Fig. 4.2 shows a sample of such optimized nonperiodic metasurface. Orange color represents the top metallization and purple represents the substrate. Each group cell contains 4×4 identical elements of $2mm$ each in size. The entire board consists of 225 optimized group cells (3600 basic elements) in total. In addition, areas close to the board edge is set to be blank to reduce possible edge effect and ensure the accuracy of element phase.

Fig. 4.3 shows the theoretical pattern calculated by the array model with elements' phase at 10 GHz. Both TE and TM patterns are normalized to their maximum beam power at all reflective angles ($-90° < \theta_r < +90°$). For both cases, there are clearly two beams located around $-30°$ (retroreflection direction) and $0°$ (normal direction). In theoretical patterns, scattering at endfire direction ($\theta_r > +70°$) is elevated to around -5 dB, since we set no

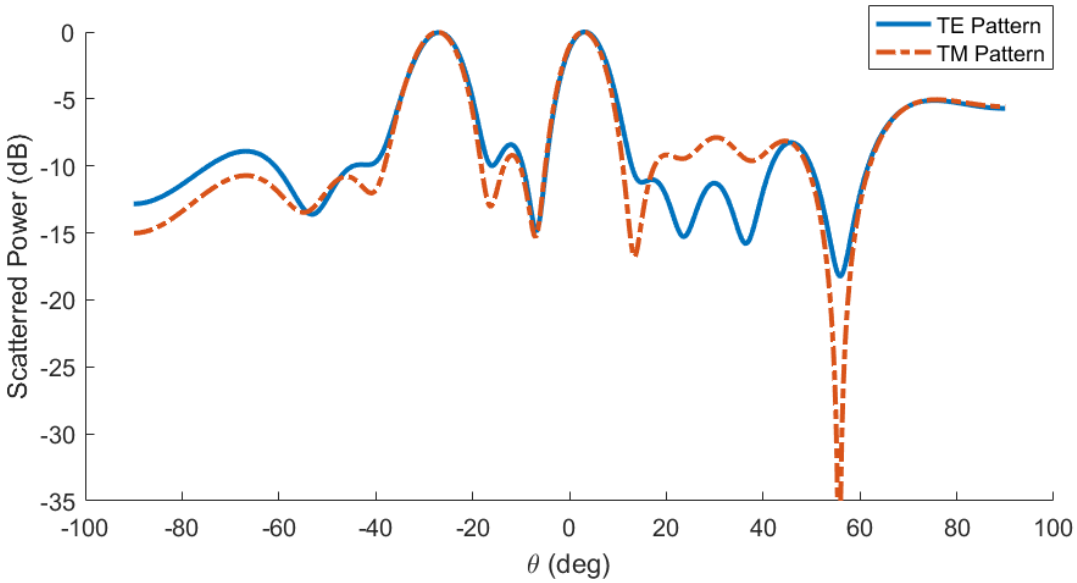

Figure 4.3: Theoretical TE/TM scattered patterns under $-30°$ oblique incidence.

constrain in the large angle scattering. However, this endfire scattering is not prominent by nature, so it is expected to be lower than reality. Other side lobes, especially those in the specular direction are suppressed under -8 dB.

Fig. 4.4 shows the simulation patterns in HFSS of the nonperiodic metasurface beam splitter at 10 GHz. Both TE/TM patterns follow the same trend as in Fig. 4.3 with two main beams at $0°$ and $-30°$.The scattering in large angles is kept at a relatively low level as predicted. For TE pattern, $-30°$ beam is 1.4dB lower than the $0°$ beam, and the side lobe near the specular direction rises to -4dB. For TM pattern, $-30°$ beam is 1.1dB higher than $0°$ beam, and other side lobes remain below -5dB.

These small discrepancies between the theoretical results and simulation emerge mainly because of the simplified array model, in which each element is characterized by its phase. In fact, there exists slight swing of reflection magnitude from 0.99 to 1 among all the elements. When using 3600 elements, such error will accumulate. Also, the mutual coupling between different group cells and the edge effect are not considered in this model. However, because

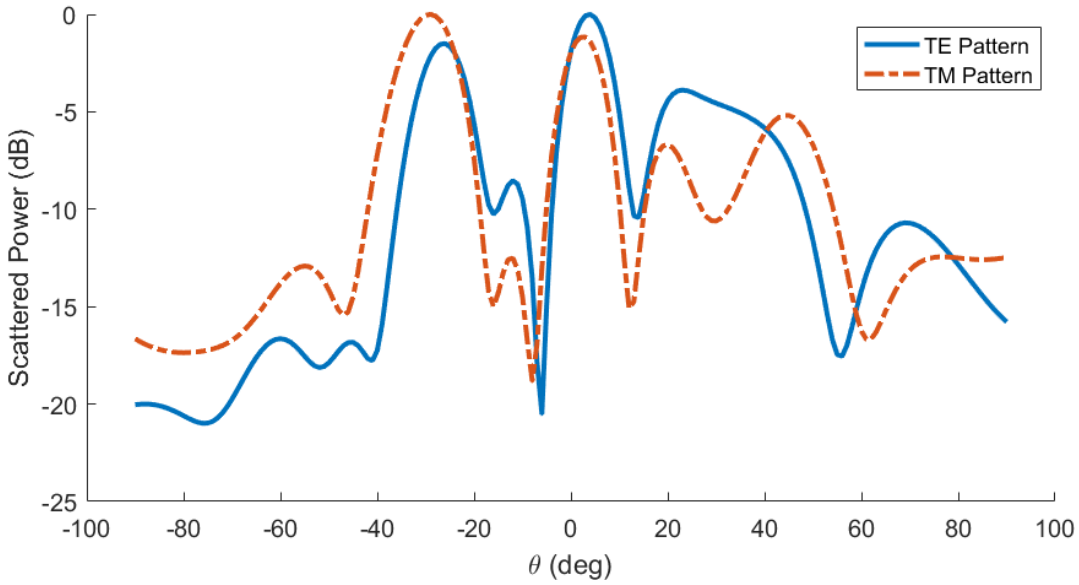

Figure 4.4: Simulated TE/TM scattered patterns under $-30°$ oblique incidence.

a great number of elements are used to construct the metasurface with periodic boundary condition inside each group cell, the scattering behavior is dominated by the 2D phased array model. Main features of theoretical patterns and simulation patterns are well matched. In addition, the optimization of this model will take only tens of minutes, while it will be almost impossible to directly optimize such a beam splitter of the same quantity of elements in any EM solver.

4.3 Measurement

This nonperiodic metasurface beam splitter is fabricated using LKPF U4 laser machine to ensure the accuracy of element size. Fig. 4.5 shows the scattered pattern for TE/TM measured in the chamber. We placed the metasurface in the far zone of a transmitter in the angle of $-30°$ and rotated the receiver from $-60°$ to $+60°$. Time gating technique is used to eliminate unwanted port reflection. Both TE and TM measured patterns show good

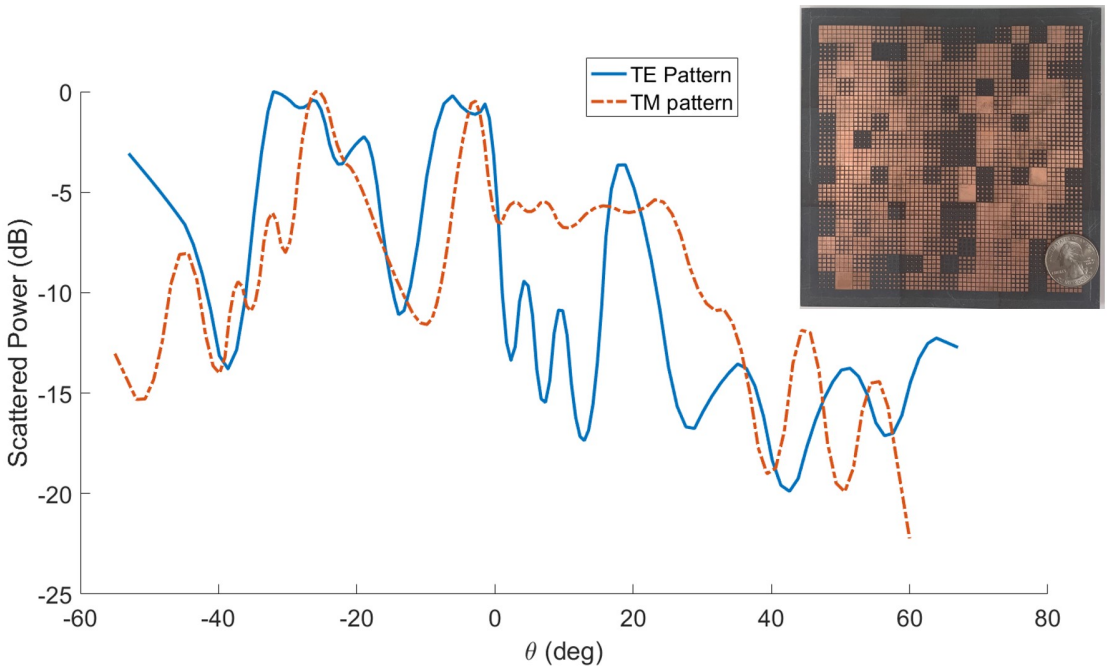

Figure 4.5: Measured TE/TM scattered patterns.

matching with simulation pattern and theoretical pattern. Two main beams can be clearly found at retroreflection direction ($-30°$) and normal direction ($0°$). For TE pattern, the beam at retroreflection angle is broadened compared to simulation result and large angle scattering (around $-55°$) is elevated. Side lobe near the specular direction are kept below -4dB. For TM pattern, the measured side lobes are all below -5dB, though the normal direction beam shifts several degrees toward the negative angles, as a result of the fabrication error or the inaccuracy of the dielectric constant of the board. This measurement verifies that main features of beam splitter is achieved by nonperiodic metasurface.

CHAPTER 5

Linear-to-Circular Polarization Converter Based on Anisotropic Metasurface

5.1 Introduction

In microwave regime, CP wave is traditionally generated by CP source antennas with slight modification from the linear polarized (LP) antenna counterpart along with various feeding arrangements [58]. The essence of CP antenna is to create two orthogonal radiating modes with 90° phase difference. However, this method may not be efficient when the communication system contains large antenna arrays considering that routing of feed lines and the fabrication complexity can be problems. An alternative way to generate CP wave is to apply a linear-to-circular polarization converter to a LP source antenna, which also has the potential to improve antenna gain and bandwidth [59]. This concept is commonly applied in the optical regime, where a quarter-wave plate made by anisotropic material is used to convert the LP wave with polarization angle of 45° to the fast axis (x-axis) and slow axis (y-axis) [60]. The phase difference of the two orthogonal polarizations will gradually accumulate when the wave travels along z-axis. When it reaches 90°, the transmitted wave will become CP wave. Assuming that the refractive indexes along x and y axes are n_x and n_y respectively, the thickness of the quarter wave plate can be determined by:

$$l = \frac{\lambda_0}{4|n_x - n_y|}, \tag{5.1}$$

where λ_0 is free space wavelength. Usually this thickness reaches several or tens of wavelengths since $|n_x - n_y|$ of common anisotropic materials (e.g. KDP in optics) is small.

Notwithstanding their popularity in optical frequencies, quarter-wave plates are less prevalent in microwave applications because they require a piece of excessively bulky material with specific anisotropic properties.

With the recent emergence of metasurfaces, people have more powerful tools to manipulate the physical behavior of the fields on the surface, such as wave front, surface impedance and magnitude/phase response. In light of the metasurface, various polarization converters of transmission type [59, 61, 62] or reflection type [63] have been realized from microwave to optical domains. In [59], a metasurface polarization converter composed of rectangular loops with diagonal microstrips has been reported. The source antenna in this design has to be placed at a short distance from the metasurface. In [61], a single layer of periodic Jerusalem cross elements has been used to achieve 4.3% simulated bandwidth. The transmission phase of this type of element can be easily tuned by changing the lengths of the cross arms. Reference [62] studies the multi-layer miniaturized-element FSS with capacitive patches and inductive wire grids and achieves desired magnitude and phase response by synthesizing the equivalent circuit model.

In this chapter, we will present transmissive stacked metasurfaces with simple geometry to convert LP wave to CP wave. This polarization converter consists of two metasurface layers with periodic Jerusalem cross elements and one interlayer with periodic square rings. Assisted by the aperture coupling interlayer, the proposed structure have the advantages of low profile, easy fabrication and good axial ratio (AR) in a relatively wide band. The performance of this metasurface prototype has been verified by both simulation and measurement in Ku band. The same design approach can also be used in other frequencies, such as THz and optics.

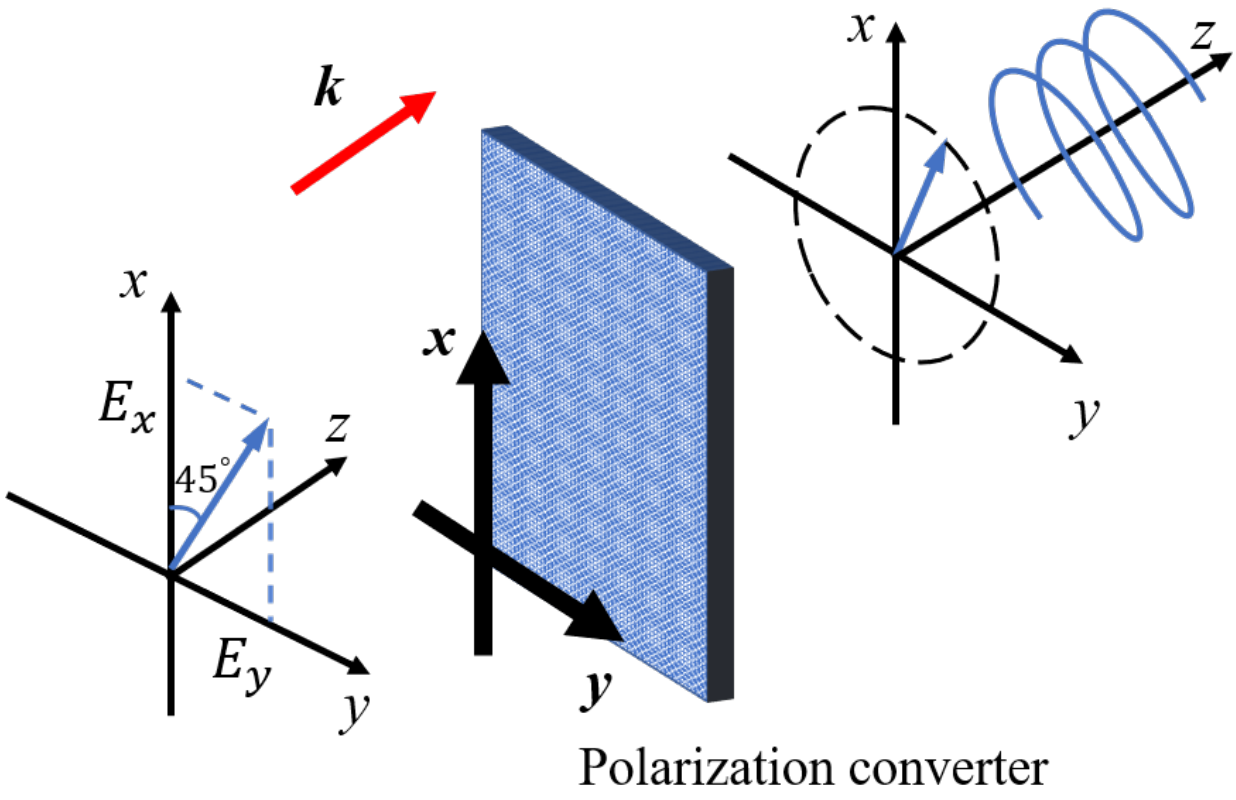

Figure 5.1: Schematic of linear-to-circular polarization converter. Incident wave polarization is 45° to the x and y axes of the polarization converter and transmitted wave is circularly polarized. Blue arrows denote the polarization of the electric field.

5.2 Theory and Methodology

Fig. 5.1 shows the schematic of a general metasurface linear-to-circular polarization converter. Similar to the quarter-wave plate, metasurface polarization converter behaves anisotropically in x and y dimensions. When the polarization of the incidence plane wave is tilted 45° with respect to the x and y axes, the incident electric field can be decomposed to $\vec{E_x^i}$ and $\vec{E_y^i}$ with equal magnitude and phase. If the transmission coefficients of metasurfaces along each polarization direction are denoted as t_x and t_y, the transmitted electric field $\vec{E_x^t}$ and $\vec{E_y^t}$ components can be expressed as:

$$\vec{E_x^t} = t_x \vec{E_x^i} \tag{5.2}$$

$$\vec{E_y^t} = t_y \vec{E_y^i} \tag{5.3}$$

In order to get CP transmitted wave, $\vec{E_x^t}$ and $\vec{E_y^t}$ should have equal magnitude and 90° phase difference. In other words, the transmission coefficients of the metasurface should satisfy:

$$|t_x| = |t_y| \tag{5.4}$$

$$arg(t_x) - arg(t_y) = \pm\frac{\pi}{2} \tag{5.5}$$

The design of metasurface therefore boils down to the design of unit cells with such transmission properties. Since the unit cell should be anisotropic along x and y dimensions for desired 90° phase difference, the $x-$ and $y-$ polarized components will experience different resonances (typically shifted resonant frequency). This usually brings out different transmission magnitude for x and y polarizations, which is the common nature of narrow band reactive impedance surface.

A low profile two-pole FSS using an aperture coupling interlayer has been proposed to achieve low in-band insertion loss with 10% fractional bandwidth[64]. Two FSS layers with

periodic subwavelength elements are used to create two poles in the filter response and the aperture coupling interlayer is used to tune the separation between the pole locations so that a flat passband is achieved. Therefore, we can insert a suitable aperture coupling interlayer into two anisotropic metasurface layers to create a feasible unit cell for the polarization converter design.

5.3 Design of the Unit Cell

Fig. 5.2 shows the schematic of the proposed unit cell. The dimensions of the unit cell are 4mm $\times$ 4mm $\times$ 2.54mm ($0.18\lambda_0 \times 0.18\lambda_0 \times 0.11\lambda_0$, f = 13.5 GHz). Two substrate layers have the same thickness h = 1.27mm with dielectric constant ϵ_r = 3.00 (Rogers RO3003). The top and bottom layers are metal Jerusalem cross elements [61], and each layer can be modeled by a shunt resonator. The arm lengths of the cross l_x and l_y are different so that the electric field polarized along x and y direction will see different lengths of metal parts and gap intervals. At the working frequency, the metasurface layers will provide capacitive reactance for one polarization and inductive reactance for the other [62]. Between these metasurface layers, there is an coupling layer composed of periodic square rings. The open aperture size r of the squre ring element controls the coupling strength of the top and bottom layers. According to the coupled resonator filter theory, top and bottom resonators will bring out two poles in transmission response and the relative locations of two poles can be changed by controlling the coupling coefficient. The aperture size r of the interlayer can be optimized to achieve desired coupling coefficient for a flat and close to unity response at the operating frequency range.

The unit cell is modeled in HFSS under periodic boundary conditions and the transmission coefficient S_{21} is simulated. The dimensions are optimized to obtain 90° phase difference as well as equal and close to unity magnitude response for two orthogonal polarizations at 13.5 GHz. The optimized parameters of the unit cell are labeled in Fig. 5.2.

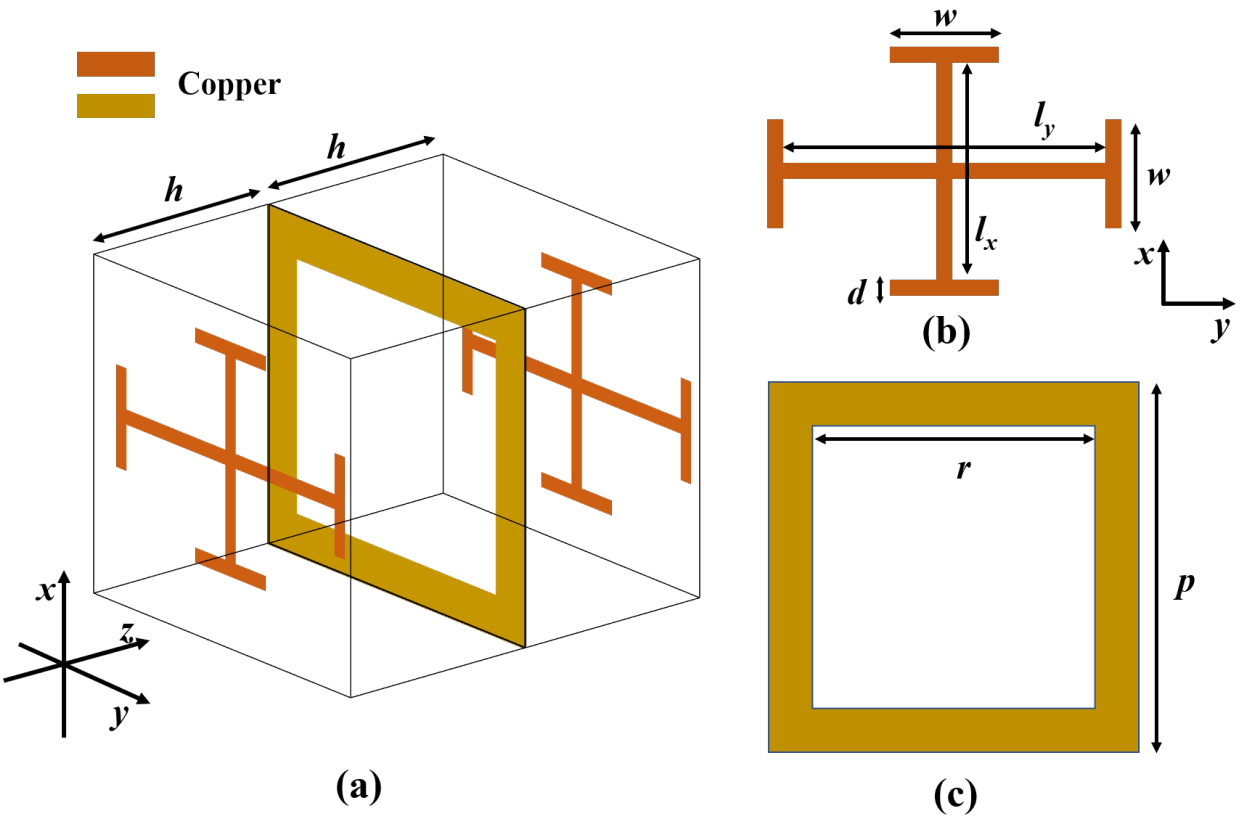

Figure 5.2: (a) Schematic of the unit cell. Copper parts are in yellow and orange color. Top and bottom layers are Jerusalem cross. Interlayer is square ring aperture. Two substrate layers are Rogers RO3003 with $\epsilon_r = 3.00$ and thickness $h = 1.27$mm. (b) Dimensions of the Jerusalem cross for frequency 13.5 GHz. $w = 1.5$mm, $l_x = 2.7$mm, $l_y = 3.2$mm, $d = 0.2$mm. (c) Dimension of the square ring aperture. $r = 3$mm. Unit cell periodicity $p = 4$mm.

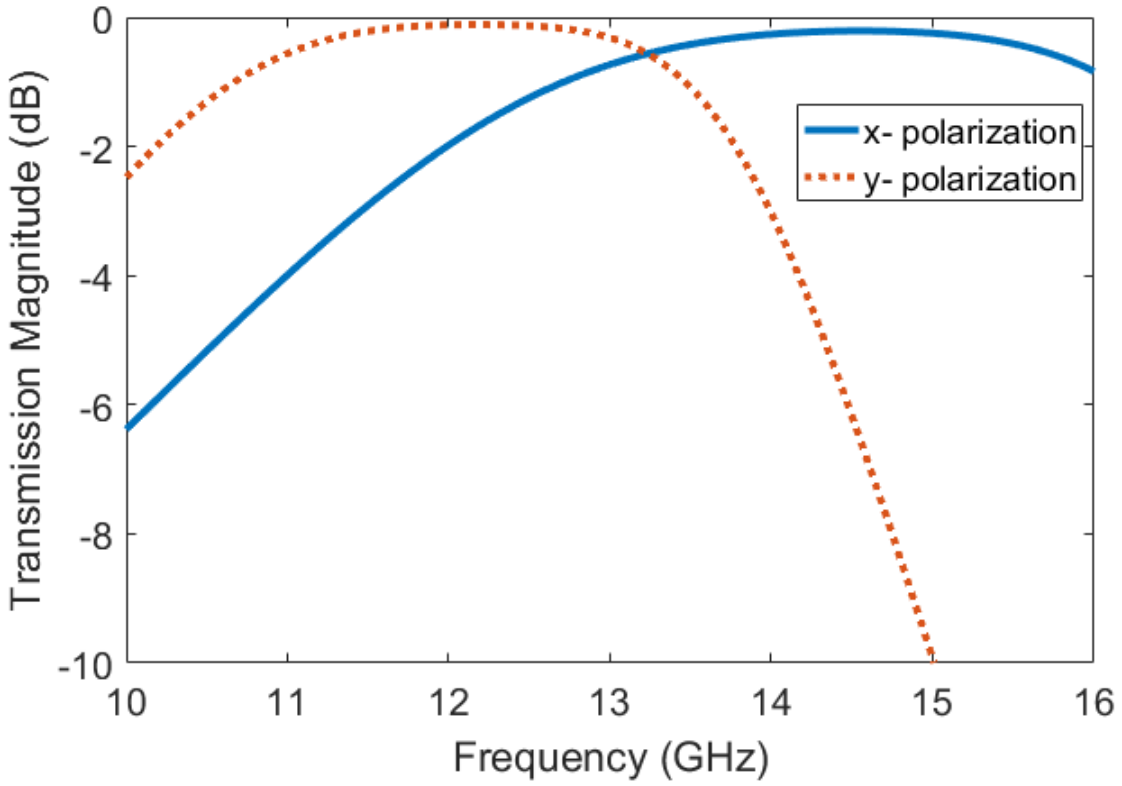

Figure 5.3: Simulated transmission magnitude of the metasurface for orthogonal polarizations.

Fig. 5.3 shows the transmission magnitude for both x and y polarizations. We find that this metasurface first behaves as two-pole polarization-dependent FSS and there exists an overlapped passband from 11.5 GHz to 14 GHz for both polarizations. In the passband around the design frequency, two orthogonal polarizations are considered to have flat and close to unity transmission response.

Fig. 5.4 shows the simulated transmission phase of the orthogonal polarizations. Note that phase difference is 90° at 13.5 GHz, which meets the CP wave requirement of equations (4) and (5). For frequencies slightly off 13.5 GHz, the phase difference indicated by the gap between the two curves will change slowly, owing to the insignificant slope difference of x and y polarizations. To evaluate the circular polarization level, AR can be calculated by the

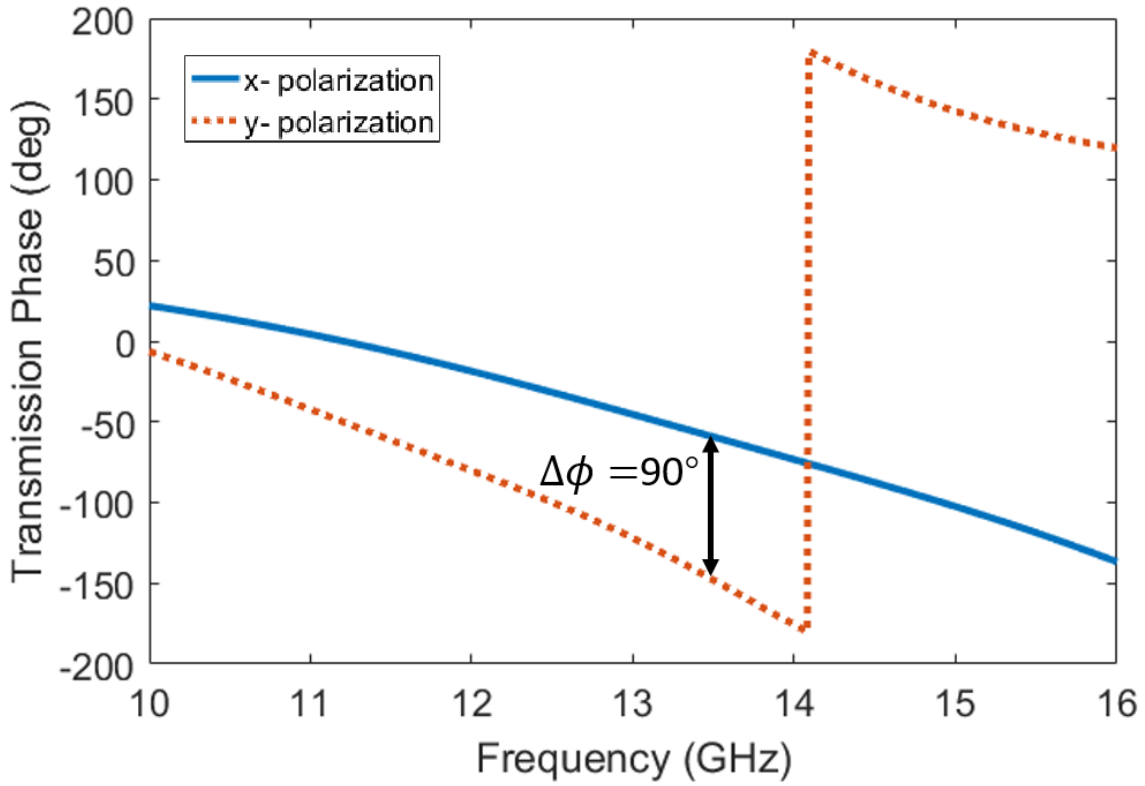

Figure 5.4: Simulated transmission phase of the metasurface for orthogonal polarizations.

magnitude and phase mismatch of transmission coefficients from equations (5.6)-(5.7) [65]:

$$AR = \left(\frac{|t_x|^2 + |t_y|^2 + \sqrt{a}}{|t_x|^2 + |t_y|^2 - \sqrt{a}} \right)^{1/2} \tag{5.6}$$

$$a = |t_x|^4 + |t_y|^4 + 2|t_x|^2|t_y|^2 \cos(2\Delta\phi), \tag{5.7}$$

where $\Delta\phi = arg(t_x) - arg(t_y)$, denoting the actual phase difference of the orthogonal polarizations.

Fig. 5.5 shows the calculated AR level. The AR level remains below 3 dB from 12.7 GHz to 13.95 GHz, which corresponds to 9.4% fractional CP bandwidth. Whereas, the reference[61] presents 4.3% simulated AR bandwidth, where the single layer Jerusalem cross elements are used with $0.10\lambda_0$ thickness. By virtue of the aperture coupling interlayer, our design improves the AR bandwidth while maintaining almost the same thickness ($0.11\lambda_0$).

5.4 Simulation and Measurement Results

A prototype of this metasurface polarization converter was fabricated using LPKF Protolaser U4 to ensure the accuracy of unit cell features. Fig. 5.6 shows the top view of the fabricated PCB metasurface. The whole board contains 1600 elements and the total size is 16cm×16cm.

The fabricated prototype was affixed in a bi-polar planar near-field antenna measurement range and was illuminated by a linearly polarized patch array feed [66]. The measurement setup is shown in Fig. 5.7, where the angle between the E-plane of the patch array and x and y axes of metasurfaces is 45°. The feed was placed at a distance of 100mm from the metasurfaces to taper the illumination to -10 dB at the rim of the board to reduce the spillover effect. The measured boresight far-field x and y components are then used to calculate the AR level through equations (5.6)-(5.7).

This metasurface polarization converter of the real size along with the LP source antenna setup is also simulated in HFSS. AR can be directly extracted from the far field in the

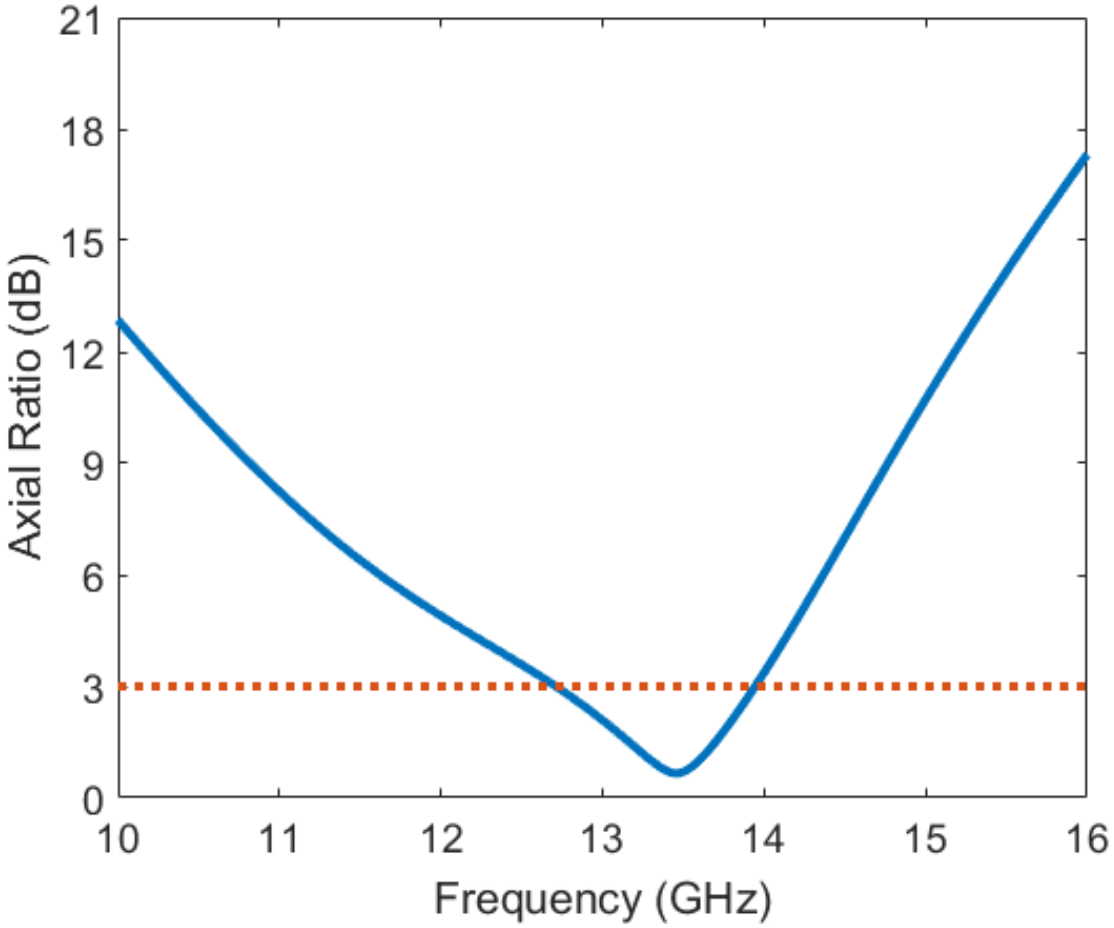

Figure 5.5: Theoretical AR of the transmitted wave through metasurface polarization converter.

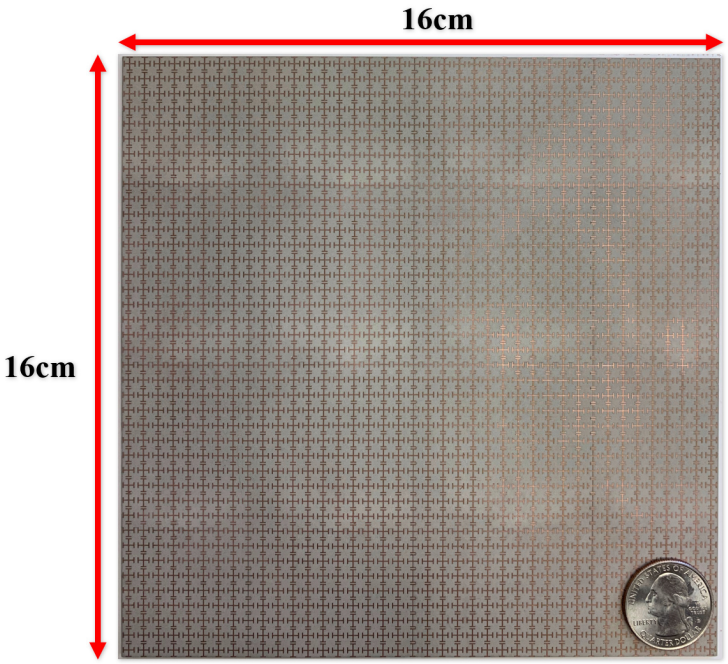

Figure 5.6: Top view of fabricated metasurface polarization converter.

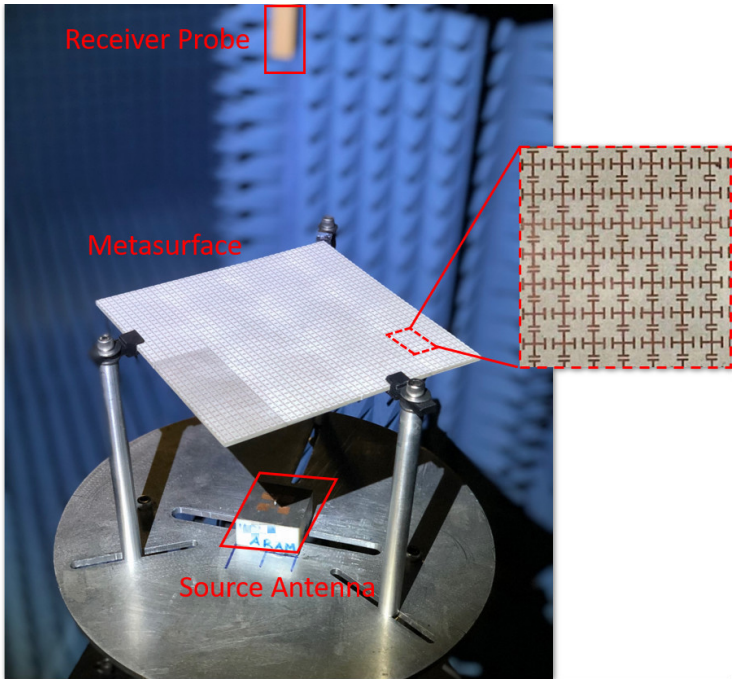

Figure 5.7: Measurement Setup.

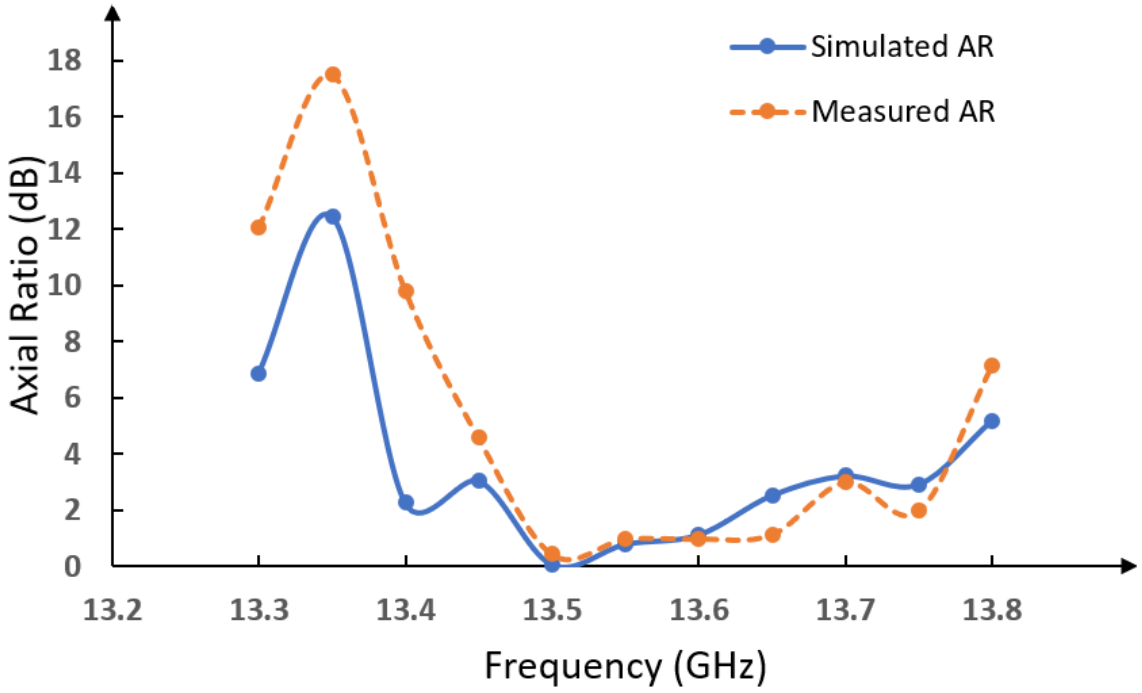

Figure 5.8: Simulated and measured AR of the transmitted wave through metasurface polarization converter.

simulation. Fig. 5.8 shows the simulated and measured AR results. Both simulation and measurement curves present close to 0 dB AR at the design frequency 13.5 GHz and follow the same trend in the measured frequency range. The simulated AR remains below 3 dB from 13.45 GHz to 13.75 GHz and measured AR bandwidth is slightly narrower. Note that the actual AR bandwidth of metasurface structure is less than that of the theoretical unit cell simulation of Fig. 5.5 for two reasons. First, the periodic boundary conditions applied in the unit cell simulation do not represent a finite-sized metasurface and do not account for spillover effect. Secondly, the unit cell simulation considers only normally incident waves, yet rays emanating from the feed impinge upon the metasurface at different angles. Discrepancies between simulated and measured results of Fig. 5.8 are attributed to implementation tolerance caused by antenna assembly, misalignment and accuracy of measurement.

CHAPTER 6

Conclusion

In this dissertation, We have studied the nonperiodic metasurfaces with various scattering properties for TE/TM or circular polarization. We have detailed the nonperiodic metasurface design procedure assisted by the optimization. The method is based on 2D nonperiodic array model, with each element characterized by its phase response. Several neighboring basic elements form a group cell to satisfy the locally periodic boundary condition. The desired scattered pattern is obtained by optimization of the group cells distribution along the surface with low computation consumption.

We first aim at the retroreflection of TE/TM wave and CP with reversed or preserved handedness. The configuration of basic element is customized considering the nature of the wave with different polarizations. Since all the cases have the same goal of enhancing the retroreflection beam while suppressing the specular scattering, they share the same cost function, regardless of the amount, shape, and the size of the elements. The full wave simulation scattered patterns match well with the theoretical optimized patterns. The measurement results validate the strong retroreflection with good efficiency.

We then demonstrate that this nonperiodic metasurface design procedure can be conveniently reproduced to implement other applications, e.g., a microwave beam splitter for TE and TM wave. The proper elements are chosen to fit the polarization of the wave. The cost function is defined to tailor the scattered pattern so that two beams at retroreflection direction and normal direction will have the same power level, with suppressed specular reflection. The full wave simulation and measurement results are presented with great match

with the theoretical pattern.

Lastly, we present a supplementary study of anisotropic metasurface-a linear-to-circular polarization converter with stacked metasurface and a coupling interlayer. The top and bottom layers of the metasurface are composed of Jerusalem cross elements for different transmission phase response of orthogonal polarizations. The interlayer is used to enhance the flat and close to unity magnitude transmission at the operating frequencies. The unit cell configuration is presented to achieve 9.3% fractional AR bandwidth. A prototype of this metasurface polarization converter has been simulated, fabricated and measured at Ku band. Both simulated and measured results agree well, showing good axial ratio around the design frequency 13.5 GHz.

All the proposed metasurface prototypes in this dissertation were implemented by PCB, attesting to their nature of low profile, inexpensiveness, and compatibility to other microwave devices or components. The designs can also be conveniently scaled to millimeter-wave, terahertz and optical frequencies.

REFERENCES

[1] D. R. Smith, J. B. Pendry, and M. C. Wiltshire, "Metamaterials and negative refractive index," *Science*, vol. 305, no. 5685, pp. 788–792, 2004.

[2] A. Grbic and G. V. Eleftheriades, "Experimental verification of backward-wave radiation from a negative refractive index metamaterial," *Journal of applied physics*, vol. 92, no. 10, pp. 5930–5935, 2002.

[3] V. M. Shalaev, "Optical negative-index metamaterials," *Nature photonics*, vol. 1, no. 1, p. 41, 2007.

[4] A. Lai, T. Itoh, and C. Caloz, "Composite right/left-handed transmission line metamaterials," *IEEE microwave magazine*, vol. 5, no. 3, pp. 34–50, 2004.

[5] C. Caloz and T. Itoh, *Electromagnetic metamaterials: transmission line theory and microwave applications*. John Wiley & Sons, 2005.

[6] N. Yu, P. Genevet, M. A. Kats, F. Aieta, J.-P. Tetienne, F. Capasso, and Z. Gaburro, "Light propagation with phase discontinuities: generalized laws of reflection and refraction," *science*, vol. 334, no. 6054, pp. 333–337, 2011.

[7] M. Silveirinha and N. Engheta, "Tunneling of electromagnetic energy through subwavelength channels and bends using ε-near-zero materials," *Physical review letters*, vol. 97, no. 15, p. 157403, 2006.

[8] P. Moitra, Y. Yang, Z. Anderson, I. I. Kravchenko, D. P. Briggs, and J. Valentine, "Realization of an all-dielectric zero-index optical metamaterial," *Nature Photonics*, vol. 7, no. 10, p. 791, 2013.

[9] C. Pfeiffer and A. Grbic, "Metamaterial huygens' surfaces: tailoring wave fronts with reflectionless sheets," *Physical review letters*, vol. 110, no. 19, p. 197401, 2013.

[10] N. M. Estakhri and A. Alù, "Wave-front transformation with gradient metasurfaces," *Physical Review X*, vol. 6, no. 4, p. 041008, 2016.

[11] D. F. Sievenpiper, J. H. Schaffner, H. J. Song, R. Y. Loo, and G. Tangonan, "Two-dimensional beam steering using an electrically tunable impedance surface," *IEEE Transactions on antennas and propagation*, vol. 51, no. 10, pp. 2713–2722, 2003.

[12] B. H. Fong, J. S. Colburn, J. J. Ottusch, J. L. Visher, and D. F. Sievenpiper, "Scalar and tensor holographic artificial impedance surfaces," *IEEE Transactions on Antennas and Propagation*, vol. 58, no. 10, pp. 3212–3221, 2010.

[13] D. Lin, P. Fan, E. Hasman, and M. L. Brongersma, "Dielectric gradient metasurface optical elements," *science*, vol. 345, no. 6194, pp. 298–302, 2014.

[14] L. Liu, X. Zhang, M. Kenney, X. Su, N. Xu, C. Ouyang, Y. Shi, J. Han, W. Zhang, and S. Zhang, "Broadband metasurfaces with simultaneous control of phase and amplitude," *Advanced Materials*, vol. 26, no. 29, pp. 5031–5036, 2014.

[15] Y. Ra'Di, C. Simovski, and S. Tretyakov, "Thin perfect absorbers for electromagnetic waves: theory, design, and realizations," *Physical Review Applied*, vol. 3, no. 3, p. 037001, 2015.

[16] C. L. Holloway, E. F. Kuester, and D. Novotny, "Waveguides composed of metafilms/metasurfaces: The two-dimensional equivalent of metamaterials," *IEEE Antennas and Wireless Propagation Letters*, vol. 8, pp. 525–529, 2009.

[17] A. Pors, M. G. Nielsen, R. L. Eriksen, and S. I. Bozhevolnyi, "Broadband focusing flat mirrors based on plasmonic gradient metasurfaces," *Nano letters*, vol. 13, no. 2, pp. 829–834, 2013.

[18] E. Doumanis, G. Goussetis, G. Papageorgiou, V. Fusco, R. Cahill, and D. Linton, "Design of engineered reflectors for radar cross section modification," *IEEE Transactions on Antennas and Propagation*, vol. 61, no. 1, pp. 232–239, 2012.

[19] C. Hawthorn, K. Weber, and R. Scholten, "Littrow configuration tunable external cavity diode laser with fixed direction output beam," *Review of scientific instruments*, vol. 72, no. 12, pp. 4477–4479, 2001.

[20] P. B. Chu, N. R. Lo, E. C. Berg, and K. S. Pister, "Optical communication using micro corner cube reflectors," in *Proceedings IEEE The Tenth Annual International Workshop on Micro Electro Mechanical Systems. An Investigation of Micro Structures, Sensors, Actuators, Machines and Robots. IEEE*, 1997, pp. 350–355.

[21] J. Liu and R. Azzam, "Polarization properties of corner-cube retroreflectors: theory and experiment," *Applied optics*, vol. 36, no. 7, pp. 1553–1559, 1997.

[22] T. Itoh and R. Mittra, "An analytical study of the echelette grating with application to open resonators," *IEEE Transactions on Microwave Theory and Techniques*, vol. 17, no. 6, pp. 319–327, 1969.

[23] C. Pon, "Retrodirective array using the heterodyne technique," *IEEE Transactions on Antennas and Propagation*, vol. 12, no. 2, pp. 176–180, 1964.

[24] R. Y. Miyamoto and T. Itoh, "Retrodirective arrays for wireless communications," *IEEE Microwave Magazine*, vol. 3, no. 1, pp. 71–79, 2002.

[25] D. S. Goshi, K. M. Leong, and T. Itoh, "A sparsely designed retrodirective transponder," *IEEE Antennas and Wireless Propagation Letters*, vol. 5, pp. 339–342, 2006.

[26] L. C. Van Atta, "Electromagnetic reflector," Oct. 6 1959, US Patent 2,908,002.

[27] V. Asadchy, A. Díaz-Rubio, S. Tcvetkova, D.-H. Kwon, A. Elsakka, M. Albooyeh, and S. Tretyakov, "Flat engineered multichannel reflectors," *Physical Review X*, vol. 7, no. 3, p. 031046, 2017.

[28] A. Arbabi, E. Arbabi, Y. Horie, S. M. Kamali, and A. Faraon, "Planar metasurface retroreflector," *Nature Photonics*, vol. 11, no. 7, p. 4151, 2017.

[29] X. Li, M. Memarian, K. Dhwaj, and T. Itoh, "Blazed metasurface grating: The planar equivalent of a sawtooth grating," in *2016 IEEE MTT-S International Microwave Symposium (IMS)*. *IEEE*, 2016, pp. 1–3.

[30] M. Memarian, X. Li, Y. Morimoto, and T. Itoh, "Wide-band/angle blazed surfaces using multiple coupled blazing resonances," *Scientific reports*, vol. 7, p. 42286, 2017.

[31] H. Tian, M. Memarian, and T. Itoh, "Electronically-tunable resonant blazed metasurface grating," in *2017 IEEE Asia Pacific Microwave Conference (APMC)*. *IEEE*, 2017, pp. 376–379.

[32] A. M. H. Wong, P. Christian, and G. V. Eleftheriades, "Binary huygens' metasurfaces: Experimental demonstration of simple and efficient near-grazing retroreflectors for te and tm polarizations," *IEEE Transactions on Antennas and Propagation*, vol. 66, no. 6, pp. 2892–2903, 2018.

[33] X. Li, C. Tao, L. Jiang, and T. Itoh, "Blazed metasurface grating with handedness preservation for circularly polarized incident wave," in *2018 48th European Microwave Conference (EuMC)*. *IEEE*, 2018, pp. 133–136.

[34] C. A. Palmer and E. G. Loewen, *Diffraction grating handbook*. Thermo RGL New York, 2002.

[35] E. Loewen, M. Nevière, and D. Maystre, "Grating efficiency theory as it applies to blazed and holographic gratings," *Applied optics*, vol. 16, no. 10, pp. 2711–2721, 1977.

[36] H. Wei and L. Li, "All-dielectric reflection gratings: a study of the physical mechanism for achieving high efficiency," *Applied optics*, vol. 42, no. 31, pp. 6255–6260, 2003.

[37] N. Destouches, A. Tishchenko, J. Pommier, S. Reynaud, O. Parriaux, S. Tonchev, and M. A. Ahmed, "99% efficiency measured in the-1 st order of a resonant grating," *Optics Express*, vol. 13, no. 9, pp. 3230–3235, 2005.

[38] C. Tao, M. Memarian, Y. Morimoto, and T. Itoh, "Non-periodic metasurfaces for blazing and beam splitting," in *2016 Asia-Pacific Microwave Conference (APMC)*. *IEEE*, 2016, pp. 1–4.

[39] Q. Wu, C. P. Scarborough, D. H. Werner, E. Lier, and X. Wang, "Design synthesis of metasurfaces for broadband hybrid-mode horn antennas with enhanced radiation pattern and polarization characteristics," *IEEE transactions on antennas and propagation*, vol. 60, no. 8, pp. 3594–3604, 2012.

[40] C. Tao and T. Itoh, "Nonperiodic metasurfaces for retroreflection of te/tm and circularly polarized waves," *IEEE Transactions on Antennas and Propagation*, vol. 68, no. 8, pp. 6193–6203, 2020.

[41] C. Tao, X. Li, and T. Itoh, "Two-dimensional non-periodic metasurface for dual polarization retroreflection," in *2018 48th European Microwave Conference (EuMC). IEEE*, 2018, pp. 1194–1197.

[42] C. Tao and T. Itoh, "Non-periodic metasurface for retroreflection of circularly polarized wave," in *2019 IEEE MTT-S International Microwave Symposium (IMS). IEEE*, 2019, pp. 35–38.

[43] C. Tao and T. Itoh, "Non-periodic metasurface beam splitter for dual polarizations," in *2019 49th European Microwave Conference (EuMC)*, 2019, pp. 670–673.

[44] A. P. C. Tao and T. Itoh, "Linear-to-circular polarization converter based on stacked metasurfaces with aperture coupling interlayer," *presented at 2020 IEEE MTT-S International Microwave Symposium (IMS)*, 2020.

[45] O. Luukkonen, C. Simovski, G. Granet, G. Goussetis, D. Lioubtchenko, A. V. Raisanen, and S. A. Tretyakov, "Simple and accurate analytical model of planar grids and high-impedance surfaces comprising metal strips or patches," *IEEE Transactions on Antennas and Propagation*, vol. 56, no. 6, pp. 1624–1632, 2008.

[46] X.-c. Wang, A. Diaz-Rubio, A. Sneck, A. Alastalo, T. Mäkelä, J. Ala-Laurinaho, J.-F. Zheng, A. V. Räisänen, and S. A. Tretyakov, "Systematic design of printable metasurfaces: validation through reverse-offset printed millimeter-wave absorbers," *IEEE Transactions on Antennas and Propagation*, vol. 66, no. 3, pp. 1340–1351, 2018.

[47] J. M. Johnson and V. Rahmat-Samii, "Genetic algorithms in engineering electromagnetics," *IEEE Antennas and propagation Magazine*, vol. 39, no. 4, pp. 7–21, 1997.

[48] D. S. Weile and E. Michielssen, "Genetic algorithm optimization applied to electromagnetics: A review," *IEEE Transactions on Antennas and Propagation*, vol. 45, no. 3, pp. 343–353, 1997.

[49] R. L. Haupt, "Phase-only adaptive nulling with a genetic algorithm," *IEEE Transactions on Antennas and Propagation*, vol. 45, no. 6, pp. 1009–1015, 1997.

[50] R. C. Hansen, *Phased array antennas*. John Wiley & Sons, 2009, vol. 213.

[51] S. S. Gao, Q. Luo, and F. Zhu, *Circularly polarized antennas*. John Wiley & Sons, 2013.

[52] C. Stanciu, F. Hansteen, A. Kimel, A. Kirilyuk, A. Tsukamoto, A. Itoh, and T. Rasing, "All-optical magnetic recording with circularly polarized light," *Physical review letters*, vol. 99, no. 4, p. 047601, 2007.

[53] J. Lee, M. Tymchenko, C. Argyropoulos, P.-Y. Chen, F. Lu, F. Demmerle, G. Boehm, M.-C. Amann, A. Alu, and M. A. Belkin, "Giant nonlinear response from plasmonic metasurfaces coupled to intersubband transitions," *Nature*, vol. 511, no. 7507, p. 65, 2014.

[54] W. Menzel, D. Pilz, and M. Al-Tikriti, "Millimeter-wave folded reflector antennas with high gain, low loss, and low profile," *IEEE Antennas and Propagation magazine*, vol. 44, no. 3, pp. 24–29, 2002.

[55] R.-B. Hwang, N.-C. Hsu, and C.-Y. Chin, "A spatial beam splitter consisting of a near-zero refractive index medium," *IEEE Transactions on Antennas and Propagation*, vol. 60, no. 1, pp. 417–420, 2012.

[56] T. Cai, G.-M. Wang, X.-F. Zhang, J.-G. Liang, Y.-Q. Zhuang, D. Liu, and H.-X. Xu, "Ultra-thin polarization beam splitter using 2-d transmissive phase gradient metasurface," *IEEE Transactions on Antennas and Propagation*, vol. 63, no. 12, pp. 5629–5636, 2015.

[57] J. R. Cooper, S. Kim, and M. M. Tentzeris, "A novel polarization-independent, free-space, microwave beam splitter utilizing an inkjet-printed, 2-d array frequency selective surface," *IEEE Antennas Wirel. Propag. Lett*, vol. 11, pp. 686–688, 2012.

[58] C. A. Balanis, *Antenna theory: analysis and design*. John wiley & sons, 2016.

[59] H. Zhu, S. Cheung, K. L. Chung, and T. I. Yuk, "Linear-to-circular polarization conversion using metasurface," *IEEE Transactions on Antennas and Propagation*, vol. 61, no. 9, pp. 4615–4623, 2013.

[60] J.-M. Liu, *Photonic devices*. Cambridge University Press, 2009.

[61] I. Sohail, Y. Ranga, K. P. Esselle, and S. G. Hay, "A linear to circular polarization converter based on Jerusalem-cross frequency selective surface," in *2013 7th European Conference on Antennas and Propagation (EuCAP)*. IEEE, 2013, pp. 2141–2143.

[62] S. M. A. M. H. Abadi and N. Behdad, "Wideband linear-to-circular polarization converters based on miniaturized-element frequency selective surfaces," *IEEE Transactions on Antennas and Propagation*, vol. 64, no. 2, pp. 525–534, 2015.

[63] M. I. Khan, Z. Khalid, and F. A. Tahir, "Linear and circular-polarization conversion in x-band using anisotropic metasurface," *Scientific reports*, vol. 9, no. 1, p. 4552, 2019.

[64] J. H. Choi, J. S. Sun, and T. Itoh, "An alternative technique in designing a low-profile two-pole bandpass frequency selective surface (FSS) using aperture coupling interlayer," in *2013 IEEE MTT-S International Microwave Symposium Digest (MTT)*. IEEE, 2013, pp. 1–3.

[65] C. A. Balanis, *Advanced engineering electromagnetics*. John Wiley & Sons, 1999.

[66] A. Papathanasopoulos, Y. Rahmat-Samii, N. Garcia, and J. D. Chisum, "A novel collapsible flat-layered metamaterial gradient-refractive-index (GRIN) lens antenna," *IEEE Transactions on Antennas and Propagation*, 2019.